POLITECNICO DI MILANO
DEPARTMENT OF CIVIL AND ENVIRONMENTAL ENGINEERING
DOCTORAL PROGRAM IN STRUCTURAL, SEISMIC AND
GEOTECHNICAL ENGINEERING

THERMOMECHANICAL BONDING PROCESSES IN MICROSYSTEMS

Doctoral Dissertation of:
Seyed Amir Fouad Farshchi Yazdi

Supervisors:
Prof. Alberto Corigliano
Prof. Aldo Ghisi

Tutor:
Prof. Stefano Mariani

The Chair of the Doctoral Program:
Prof. Umberto Perego

2020 – Cycle XXXII

I had the good fortune of having more than one good teacher who shaped my thoughts. The lessons of a good teacher remain etched in my soul. With these emotions and feelings, I would like to thank them all.
I would like to offer my sincere gratitude to my supervisors, Prof. Alberto Corigliano and Prof. Aldo Ghisi, from whom I learned immensely during my studies. Their support and encouragement helped me through this journey and are truly appreciated.
A wishful thank to STMicroelectronics for supporting this project financially and defining this project by which, I stepped into the world of microsystems production. Also a special thank to Dr. Matteo Garavaglia whose incredible knowledge and gracious efforts make this research proceed.
I am so fortunate to have all the support and the courage given by my love, my dearest Shirin, who has been standing beside me in all ups and downs and has made me a better person, since she came to my life.
Last but not least, I am grateful to have such wonderful family and friends that I am proud of and deserve much more appreciation that I could say here.

I dedicate this dissertation to the people of my homeland, although I am far from them geographically, my mind is always with them and my heart is always beaten for them.

Abstract

MICROSYSTEMS production consists of several stages, one of which is dedicated to packaging. Silicon wafer-level bonding is the main part of packaging and it is intended to protect the delicate parts of the systems as well as to maintain the hermiticity of the MEMS chamber.
The main problem existing in this process is the residual stress. Hence, the aim of this thesis is to identify the sources of the residual stress and to present a solution to decrease it. In order to achieve this goal, first the effect of thin film deposition on the residual stress is studied. In the next step, the binding material, i.e. glass frit, is characterized. Microstructural features and composition are studied by scanning electron microscopy and energy dispersive X-ray spectroscopy, respectively. Mechanical properties are measured by nanoindentation tests and the surface topography and its characteristics are obtained by laser profilometry.
Also, the quality of bonding by means of mechanical resistance to external loads is investigated by die shear test. The failure mechanisms are studied experimentally as well as numerically, by exploiting the cohesive zone model for fracture.
The whole thermomechanical process of wafer bonding is then modelled and simulated via a finite element commercial code. The sources of the residual stress are recognized by the results of the simulations, in terms of the effect of thermal expansion coefficient difference as well as the effect of mechanical constraints.
Finally, a solution to decrease the warpage of bonded wafer is introduced via a new micromachining process. By reducing the thickness of both

wafers at the center, the effect of the thermal expansion coefficient difference as well as mechanical constraints in bonding process is lessened. The simulation results show the new wafer configuration decreases 34% of wafer warpage.

Sommario

La produzione dei microsistemi contempla molti passaggi, uno dei quali è dedicato all'incapsulamento o packaging. L'incollaggio di fette di silicio è il passo principale a livello di packaging e ha l'obiettivo sia di proteggere i componenti più delicati del sistema sia di mantenere l'ermeticità della camera dove è posizionato il microsistema.
Il problema principale del processo è lo sforzo residuo. Dunque, l'obiettivo di questa tesi è di riconoscere le cause e presentare delle soluzioni in modo da ridurre lo sforzo residuo.
Innanzitutto, viene studiato l'effetto della deposizione di film sottili sulla fetta di silicio. Poi, il materiale dell'incollaggio, detto "glass frit", è caratterizzato mediante un microscopio elettronico a scansione (SEM) e mediante spettroscopia EDX; la topografia del materiale è misurata con una profilometria a laser. Per valutare la resistenza dell'incollaggio, si esegue una prova di nano-indentazione sul glass frit. La resistenza meccanica dell'incollaggio è misurata con un test di taglio sul "die" di silicio; i meccanismi della frattura sono quindi studiati sperimentalmente.
Utilizzando un modello di frattura coesiva, i risultati ottenuti sperimentalmente sono riprodotti anche numericamente. Infine, sfruttando il metodo degli elementi finiti, il processo di incollaggio viene simulato in tre dimensioni, con le medesime condizioni che si adottano nel processo industriale. Lo spostamento fuori piano è confrontato con le misure sperimentali e il paragone risulta essere in buon accordo. Inoltre, con questo modello ad elementi finiti viene introdotto un nuovo processo di micro-fabbricazione per ridurre la curvatura delle fette. Il processo consiste nel limitare lo spes-

sore al centro della fetta di silicio, così diminuendo l'effetto della differenza nel coefficiente di espansione termica fra silicio e glass frit. Le analisi numeriche mostrano un 34% di decremento dello spostamento fuori piano nella nuova configurazione.

Contents

List of Acronyms

BTT	Barrier trench technology
CTE	Coefficient of thermal expansion
CVD	Chemical vapor deposition
CZM	Cohesive zone model
DC	Direct current
DOF	Degree of freedom
EDX	Energy dispersive X-ray spectroscopy
FE(M)	Finite element (method)
HF	Hydroflouric acid
IC	Integrated circuit
IMC	Intermetallic compound
MEMS	Micro-electro-mechanical systems
PVD	Physical vapor deposition
SEM	Scanning electron microscopy
TEM	Transmission electron microscopy
TLP	Transient liquid phase
UHV	Ultra high vacuum
UV	Ultra violet
WLP	Wafer level packaging

CHAPTER 1

Introduction

1.1 Overview of the problem

Several steps participate in microsystem production, starting from the deposition of silicon oxide and photo-sensitive layers, then the lithography process follows by deep reactive-ion etching in order to remove the excessive parts. After creating the mechanical structures of the microsystems such as beams or actuators, it is necessary to protect these fine parts from external hazards, either in further steps of manufacturing or in the working condition. Here, the first level of packaging, known as wafer-to-wafer bonding, is performed. There are various methods in the industry to perform this process, such as i) direct bonding assisted by temperature only, ii) anodic bonding using electric field, or iii) exploiting a third material as the binder between silicon wafers.
Since there are different materials used for microsystem packaging at different levels, due the difference in the thermal expansion coefficient of these materials, a residual stress arises in the structure. Different level packaging leads to the accumulation of this stress and to mechanical failure. Therefore, the minimization of the residual stress and its induced deformation is one of the challenges that the MEMS industry is struggling with nowadays.

1.2 Objectives

In order to overcome the issues related to silicon wafer bonding mentioned in the previous section, the following goals have been defined in this thesis:

- comprehension of the bonding process steps;
- characterization of the binding material, i.e. glass frit;
- analytical study of the thin film and its effects on the substrate during bonding;
- modelling of the whole thermocompression bonding process;
- developing of a solution to reduce the warpage;
- mechanical analysis of the bonded die in order to measure the bonding reliability.

1.3 Methodology

In order to achieve the objectives of this doctoral thesis, as initial step, the previous researches from academic books and journals were studied. Next, the study of the bonding machine and the understanding of the steps and parameters affecting the bonding were done. According to the literature review, there was a lack of some experimental data on glass frit. To compensate, a set of experimental tests at different length scales were designed and performed. Then, by using the results of the experiments, the bonding process was modelled and simulated using a commercial FE code, which helped to discover an idea to solve the problems which always accompanied the glass frit bonding process.

1.4 Organization of the dissertation

In this dissertation, in the Chapter 2 microsystems and their production processes as well as different types of wafer-to-wafer bonding are introduced. In the Chapter 3, as a possible insight on the order of magnitude of the induced stress, the Stoney formula derivation and bow calculation as well as the effect of the film thickness on the final curvature are discussed. In the same Chapter, the effect of glass frit film on the curvature of the silicon wafer is calculated. Furthermore, the three-layer configuration is analytically studied.

Next, Chapter 4 is dedicated to the characterization of the glass frit material. Laser profilometry, to measure the surface topography, nanoindentation, to obtain the mechanical properties, and SEM analysis, to observe the microstructural features, are discussed.
In order to evaluate the reliability of the dies bonded with glass frit, the die shear test is performed. The effect of the test parameters on the test results and the failure mechanisms are investigated in Chapter 5. Furthermore, the Cohesive Zone Model (CZM) is described in this Chapter; by exploiting this model, the die shear test and the crack propagation are modelled.
In Chapter 6, the FE model of the whole thermomechanical process for glass frit bonding is presented. The results help to identify the sources of the residual stress, and suggest to propose a solution to decrease the residual stress and wafer bow, discussed in Chapter 7. By introducing a thickness reduction step to silicon wafers, before the bonding process, a significant warpage reduction is foreseen. To verify this solution, the results of the bonded wafers according to the new configuration are also presented in this Chapter.
Conclusions are drawn in Chapter 8, where possible further research objectives are also suggested.

CHAPTER 2

Wafer Bonding in Microsystem Production

2.1 Introduction

MEMS is an acronym standing for micro-electro-mechanical systems. The first letter (M) indicates the size of the devices. The length of the parts in these devices is on the order of microns (one-millionth of a meter). The E (electro) refers to electricity, often in the form of electrostatic forces. The second M (mechanical) refers to the movable parts of the devices and the last one, S (systems) indicates that the electric and mechanical parts are forming a system working together [1]. Due to the fact that the feature size of the MEMS is in microns, they are also known as microsystems. In order to give an estimation about the size of these systems, Figure 2.1 shows a perspective of the size of a device; 16 9-axis MEMS devices can be placed on a one cent European coin. Microelectromechanical systems (MEMS) have influenced many industries. As meaningful examples, microscale accelerometers are used to monitor structures, micromirrors have been adopted in laser scanners and 3D imaging, gyroscopes in inertial navigation and control systems and micropumps in biomedical applications [1]. Smart utilization of the phenomena, which are dominant at micro-scale and neglected at macro-scale, creates devices with completely different work-

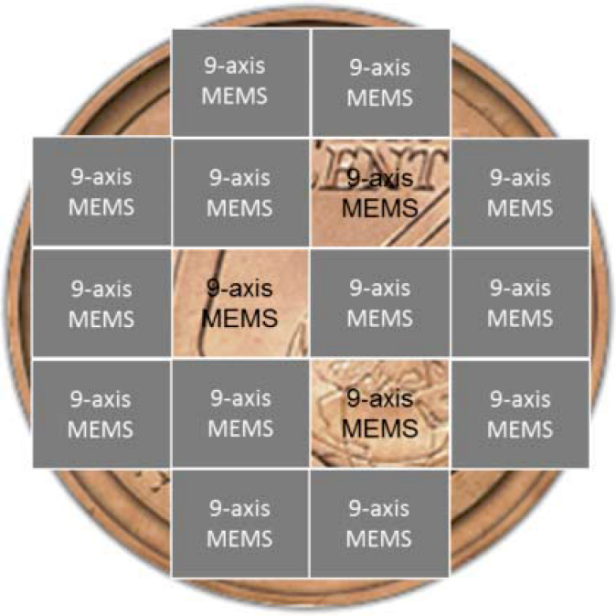

Figure 2.1: *Size scale comparison of a MEMS device and a 1 cent coin [1]*

ing principle. Also, the fabrication of devices with such small geometrical features needs special instruments and procedures.

2.2 Microsystem Production Process

Figure 2.2 shows the steps of manufacturing a flexible diaphragm, used in a pressure sensor. The initial step starts from a thin silicon plate, known as silicon wafer. The most common silicon wafer used in microsystem production is monocrystalline in either 4 or 8 inches diameter (525 or 725 μm in thickness, respectively). Since silicon is an anisotropic material, it has different properties in different crystallographic directions (see Figure 2.3). The microsystem industry takes advantage from this feature, e.g. for anisotropic etching, which is described later in this Section. As presented in Figure 2.4, a silicon wafer could have the grain orientation aligned to <100> or <111> crystallographic direction.

2.2.1 Film Deposition

First, a thin layer of SiO_2 is deposited on the wafer. This layer is also an electrical insulation layer which separates the wafer from the electrical sec-

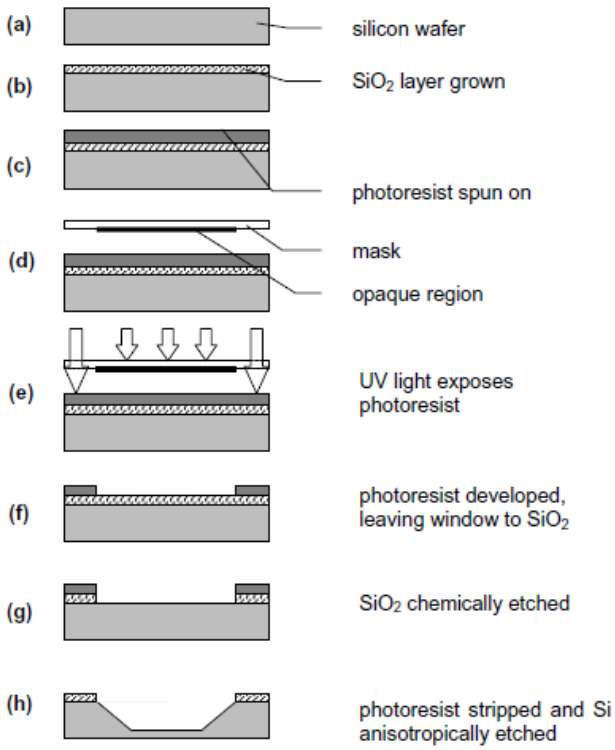

Figure 2.2: *Steps in a bulk micromachining process [2]*

tion of the MEMS. This silicon oxide layer, known as *native oxide layer*, is 20-30 nm in thickness. In order to deposit an oxide layer as a sacrificial one, a larger thickness is required. Hence, via *dry oxidation* or *wet oxidation*, at an elevated temperature between 800 to 1200 °C, with controlled oxygen flow in the furnace, an oxide layer with the thickness 100 nm-1.5 μm is grown on the substrate. The difference between dry and wet methods is that, in the latter, water is used to react with silicon instead of oxygen. The time of the oxidation process to achieve the desired thickness is governed by oxidation kinetics. Models such Deal-Grove [3] (see Equation 2.1) is mostly used to calculate the reaction time:

$$x_{ox} = \frac{A}{2}\left\{-1 + \sqrt{\frac{4B}{A^2}(t+\tau)+1}\right\} \tag{2.1}$$

where x_{ox} is the oxide thickness, A and B are temperature-varying constants, t is the oxidation process time and τ is a parameter depending on

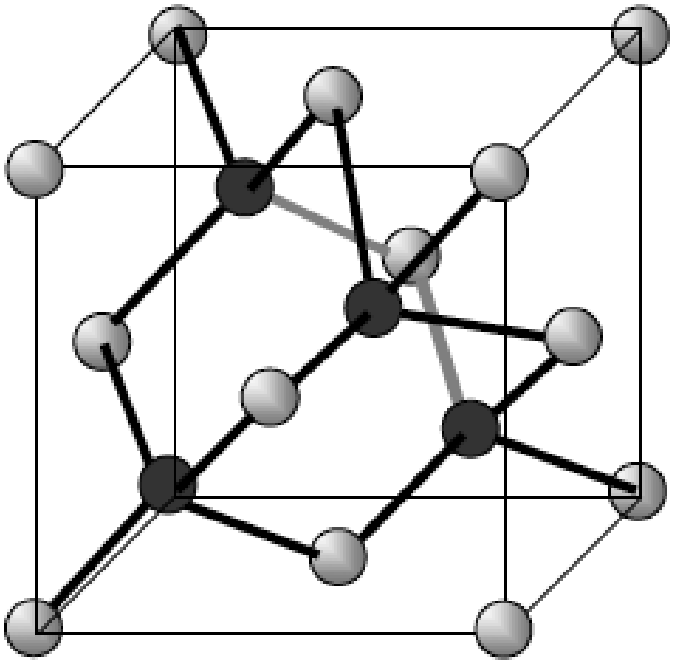

Figure 2.3: *Silicon crystal unit cell [2]*

the initial thickness of the oxide.
There are various techniques to add different layers above the oxide layer. One of which, physical vapor deposition (PVD), is based on the vaporization of a pure material in order to expose the substrate to the wafer. This process is mostly done in a vacuum environment. A flux of the evaporated material goes to the substrate and is attached to it. The other method is chemical vapor deposition (CVD), in which a chemical reaction takes place on the substrate between the gas phases sent toward the substrate. Electrodeposition is another technique for thin film deposition. By an electrical field, metal ions solved in a electrolyte are deposited on the surface. In order to deposit polymers, spin casting is used, where a solution is distributed on the wafer via centrifugal force.
By utilizing the methods described above, different parts of the MEMS structure or the layers which will be removed later are deposited on the silicon substrate. One of these sacrificial layers is a photosensitive layer in order to perform the lithography process, discussed in the next Section.

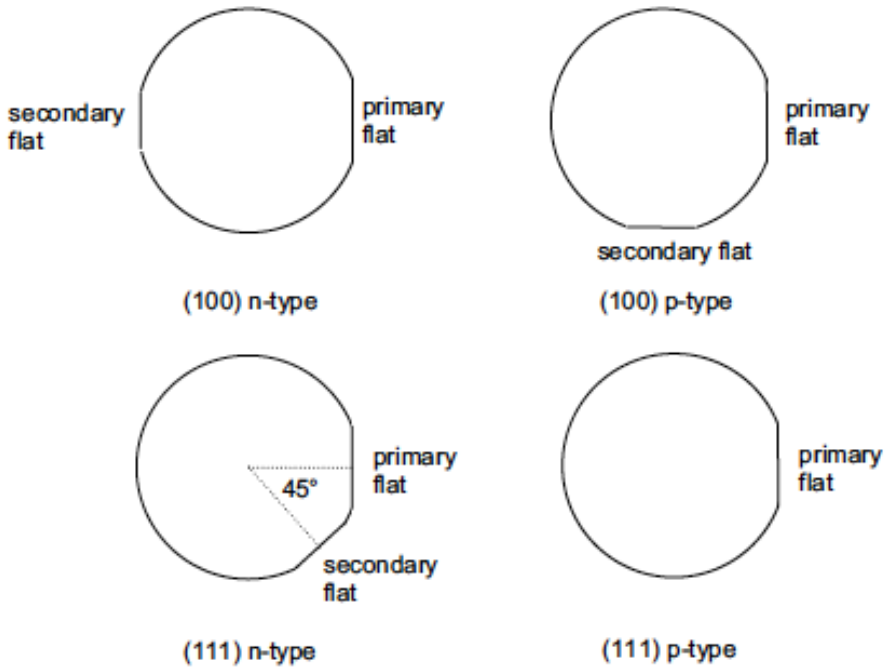

Figure 2.4: *Silicon wafer orientations [2]*

2.2.2 Lithography

Lithography is defined according to Merriam-Webster dictionary [4] as follows:

Definition 2.2.1. *The process of printing from a plane surface (such as a smooth stone or metal plate) on which the image to be printed is ink-receptive and the blank area ink-repellent.*

However, in MEMS production, lithography transfers structural patterns from a mask to the silicon wafer. As discussed in the Section 2.2.1, a layer of photosensitive material is coated above the silicon oxide film. The photosensitive layer is categorized to positive resist, where the parts exposed to UV light are more soluble, or negative, where the parts exposed to UV light are less soluble. In the next step, the mask containing the pattern of the structural part is used, in order to transfer the structural design to the photosensitive film. There are three different methods to transfer the pattern: i) contact printing, ii) proximity printing, and iii) projection printing. In contact printing, the mask touches physically the resistive film and presses against it. In this method, the pattern is transferred in a simple process, but

the mask can be used only a few times before the patterns are destroyed. Metal coated masks last more with respect to the gelatin ones. Cleanliness of the masks is the other issue as they in are in contact with the wafer.
In proximity printing, there is a small gap (between 10-50 μm) between the mask and the resistive film. Although the durability of the masks is higher than in the contact printing method, the gap is causing diffraction, which leads to poorer resolution. Contact printing and proximity are also known as shadow printings, due to the opaque and transparent regions made by these methods. The theoretical resolution for contact and proximity printing is [5]:

$$\begin{aligned} R &= \frac{3}{2}\sqrt{\frac{\lambda z}{2}} \qquad \text{Contact printing} \\ R &= \frac{3}{2}\sqrt{\lambda s} \qquad \text{Proximity printing} \end{aligned} \tag{2.2}$$

where λ is the wavelength of the exposing radiation, z is the thickness of the photoresist and s is the gap between the mask and the photoresist surface.
In the projection method, instead, by utilizing several optical components, the mask pattern is projected precisely on the wafer. The lifetime of the mask in this method is nominally infinite. The other advantage is that the pattern can be transferred by different magnifications. As depicted in Figure 2.5, the system contains a light source, a condenser lens, the mask, the objective lens and the wafer. The condenser lens owns a series of glass lenses and/or mirrors. The purpose of the condenser lens system is to deliver the light uniformly to the mask, while the objective lens gathers the diffraction patterns and transfers it to the film. The objective lens system also contains more than 20 lenses in order to reduce the geometrical aberrations. Assuming a single objective lens, the relationship between the source and target distances to the focal length of the lens is obtained by the following equation [2]:

$$\frac{1}{s} + \frac{1}{s'} = \frac{1}{f} \tag{2.3}$$

where s is the object distance from the lens, s' is the image distance, and f is the focal length of the thin lens. The last important parameter is the wavelength of the source that can extend the diffraction limit.

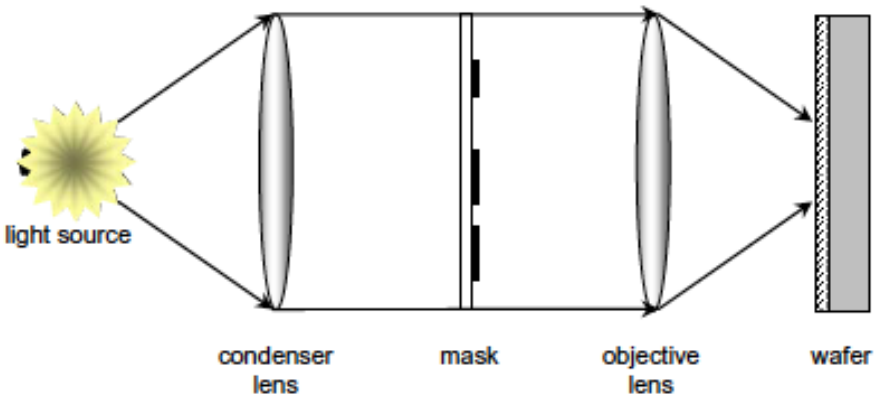

Figure 2.5: *Sequence of parts in projection lithography [2]*

2.2.3 Micromachining

Micromachining can be divided into *bulk micromachining* and *surface micromachining*. In bulk micromachining, the unwanted parts are removed from the substrate, while in surface micromachining, the sacrificial layers are removed in order to achieve the final structure. Figure 2.6 shows a sample of surface micromachining.

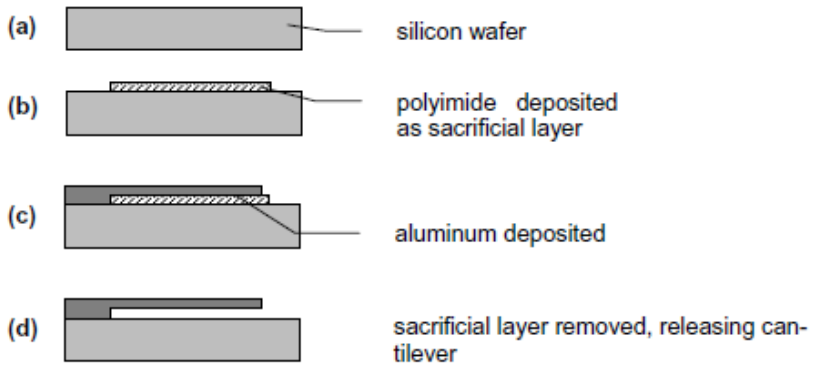

Figure 2.6: *Surface micromachining [2]*

The material removal is achieved through chemical etching, where a chemical solution dissolves the material. Etching process can be performed either by liquid solution known as wet etching, or by reactive compounds in gas phase, which is called dry etching. The etching process can be isotropic or anisotropic; in the isotropic one the etching rate (i.e. length of mate-

rial removed over time) is equal in every direction; in the anisotropic one, the etching rate is different along different directions. In Figure 2.2, the removal of the photosensitive and silicon oxide layers is isotropic, but the silicon substrate is anisotropically etched.
Another difference is that the etchants (etch solutions) are mostly alkaline for anistropic etching and acidic for the isotropic one. Table 2.1 shows different etchants for isotropic and anisotropic etching. In Table 2.1, {111}

Isotropic	
Etchant	Application
48% HF	SiO_2
Poly etch $HF/HNO_3/HC_2H_3O_2$	Si
Anisotropic	
Etchant	{111}/{100} selectivity
KOH (40-50 wt%)	100:1
Tetramethylammonium hydroxide (22 wt%)	50:1

Table 2.1: *Bulk micromachining etchants*

and {100} indicate the silicon crystallogrphic plane directions [2] [5].
Dry etching, in contrast with wet etching which delivers the etchant in aqueous solution, uses gasous form or ionized ions. In dry etching, the gas bombards the surface resulting in physical and chemical etching mechanism. The example of dry etchant is xenon diflouride (XeF_2). It can etch silicon without any effect on the metal parts of the structure, which makes it valuable for surface micromachining.

2.3 Wafer-Level Packaging

The next step in microsystems production is packaging. The packaging process for MEMS has its own features in comparison with IC packaging. At 0-level packaging, the aim is to provide a hermetic environment to protect the delicate structures during manufacturing and use, which is obtained by *Wafer-level Packaging (WLP)*. 1^{st}-level packaging is instead semi permeable to chemicals, but the important factor is controlling the moisture. At the last stage, 2^{nd}-level packaging, electromagnetic interference protection, to prevent stray signals from or to the device, has to be guaranteed [6]. Therefore, the packaging cost could reach up to 70% of the total cost [7]. In order to to protect the micromachined silicon wafer during the dicing process, a wafer level packaging is performed by encapsulating it with another silicon wafer. As primary step, the stack of two or more wafers are aligned by optical sensors on the wafer alignment machine and the alignment keys.

Then, the wafers are taken to the chamber for the bonding step. There are different methods for WLP, they are discussed in the following subsections.

2.3.1 Direct Bonding

Silicon Direct Bonding, also known as Silicon Fusion Bonding or Silicon Thermal Bonding, consists into joining two silicon wafers in contact without an intermediate layer and without external force. This method can be used both with high and low temperature and the wafers are bonded via Van der Waals forces, hydrogen bonding, capillary forces or electrostatic forces [8]. In theory, every two wafers can be bonded in this way under the condition of flat surface. However, it is not always possible, since it is important to activate the surface before bonding by wet chemical cleaning. Based on the chemicals of the surface, the bonding can be subdivided into *hydrophilic* or *hydrophobic*.
In hydrophilic bonding, there is a thermally induced oxide layer on one silicon wafer and a native oxide layer on the other. The hydroxyl groups (–OH) in the hydrophilic silicon wafers are polarized and the bond is initially created through the molecules of the water. During annealing the molecules of the water dissolve into the surrounding materials or form silanol groups (Si-OH) on the surface. Finally, the bond is obtained between silanol groups with this chemical reaction:

$$\mathrm{Si{-}OH + Si{-}OH \longrightarrow Si{-}O{-}Si + H_2O} \tag{2.4}$$

Figure 2.7 demonstrates the Stengl's model [9] for hydrophilic silicon direct bonding. In the hydrophobic bonding, instead, the native oxide layer is removed by hydrofluoric acid, which remains on the surface with Si-H and Si-F groups. In the presence of water, the Si-F group is substituted by Si-OH, but the Si-H group is making a hydrophobic surface. In this method, at the temperature of 150-300 °C, a bridge is formed between wafers by the hydrofluoric molecules. At the annealing temperature (300-700 °C), according to the following reaction, hydrogen desorbs and a Si-Si bond forms.

$$\mathrm{Si{-}H + Si{-}H \longrightarrow Si{-}Si + H_2} \tag{2.5}$$

The hydrophobic bonding is more sensitive to the roughness due to lack of water molecules between the wafers.
Direct bonding can be also performed at low temperatures as if the wafers are pre-processed and susceptible to high temperatures. The most popular low-temperature bonding is hydrophilic plasma activated bonding. In this method, the surfaces of one or both wafers are activated with a short

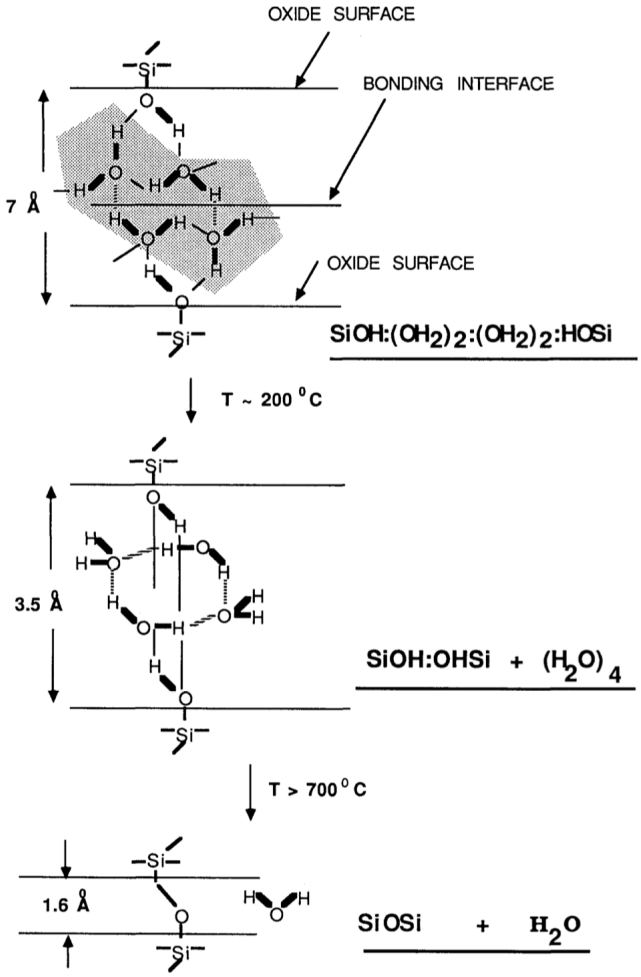

Figure 2.7: *Formation of silicon boding mechanism [9]*

plasma treatment before the bonding process. Further processes for low-temperature bonding have been reported, like argon beam activation based bonding [10], UHV hydrophobic bonding [11] and ultraviolet ozone activation bonding [12]. The main disadvantages of direct silicon bonding are very high bonding temperature, hydrogen diffusion in the silicon, the presence of voids at the bonding area due to water evaporation and complex pre-process (e.g. surface preparation). As a result, this method is not commonly used in recent years.

2.3.2 Anodic Bonding

Electrostatic bonding or anodic bonding is a low-temperature (below 500 °C) bonding method in which the process is assisted by an electric field. The method was introduced by Wallis and Pomerantz [13, 14] in 1968. In comparison to direct bonding, anodic bonding is less sensitive to the surface roughness. On the other hand, due to the presence of a high electric field, there is the possibility to harm the microelectronic parts of the device. The principle of the anodic bonding is based on the polarization of alkali-containing glasses by applying a high DC voltage (400-1000V), while the wafers are on a hot plate with temperature between 350-450 °C. The alkali cations are moving toward the cathode, consequently an alkali-depleted region is made near the anode. A very high electric field at the periphery of the contact points pulls the nearest regions together and viscous flows of the glass make the wafers come into close contact. Large electrostatic field at the depletion layer creates a substantial electrostatic pressure, maintaining the wafers into contact. Then, chemical reactions at the interface lead to the oxidation of the silicon and atomic bonds between wafers.
The quality of the bonding depends on the presence of the hydroxyl group or the oxygen in other forms (in the bonding atmosphere [15] or oxygen plasma treatment [16]) on the surface of the wafers. The increase in the oxidation layer thickness as well as the air gap between the wafers, as demonstrated in Figure 2.8, decreases the electrostatic pressure. By increasing

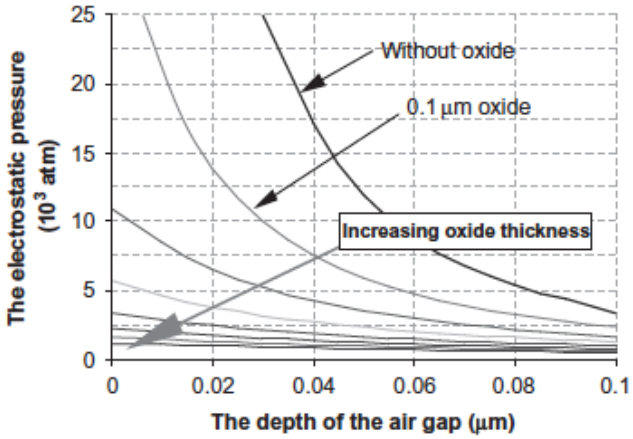

Figure 2.8: *Effect of air gap and thickness of the oxide layer on the electrostatic pressure of anodic bonding with depletion layer thickness of 0.1 μm [6]*

the temperature and the voltage, the bonding time decreases. However, at atmospheric pressure, the gas breakdown might happen. The theoretical maximum voltage that can be applied without gas breakdown can be calculated by Paschen's law [17]:

$$V_B = \frac{Bpd}{ln(Apd) - ln(ln(1 + \frac{1}{\gamma_{se}}))} \tag{2.6}$$

where V is the breakdown voltage, p is the pressure, d is the gap distance, γ_{se} is the secondary-electron-emission coefficient, A is the saturation ionization in the gas at a particular E/p (electric field/pressure), and B is related to the excitation and ionization energies. Constants A and B are obtained experimentally and are approximately constants for every E/p for each gas.
The bonding process is monitored by the electric current. There is an initial peak resulting from the increment of the contact area, then the current decays continuously until a plateau, which means the bonding process is complete.

2.3.3 Intermediate Layer Bonding

The last category of WLP includes a third material as an intermediate layer to bond wafers. Eutectic alloys, soft metals, polymers, glasses and solders can be used as the middle layer in this method.

2.3.3.1 Solder Bonding

Bonding with solders occurs at low temperature and due to kinetics of the solders, the wetting process takes some minutes. At the elevated temperature, solder fills the gaps and nonplanarities, hence this method needs low bonding pressure. During cooling down, the stress is reduced by material creep. The common solder used is SnAg with 0.5% Cu. The solder is applied on the wafer by electroplating, stencil plating or sputtering. Uncontrolled material deposition might lead to overflow of the solder squeezing-out at the high temperature and consequently, decreasing the bonding yield. Although the solder bonding is hermetic, oxygen, hydrogen and water outgassing from microcavities is reported. [18].

2.3.3.2 Eutectic Bonding

In this method, bonding between a pair of wafers is formed by exploiting the eutectic point of a binary metallic alloy. The eutectic point is at a certain composition and temperature, where two solids form simultaneously from a single liquid phase [19]. The binary systems used in this process are Au-Si, Au-Sn, Al-Ge, Cu-Sn and Au-Ge. The metal ring on the wafer, in particular, is made of Au-Si. The bonding mechanism can be divided to

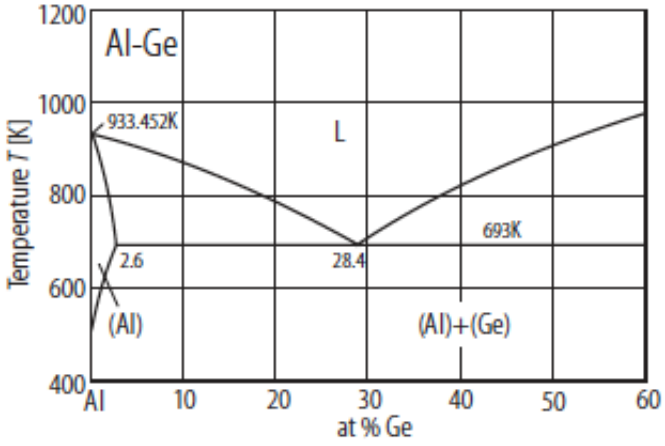

Figure 2.9: *Aluminum-Germanium phase diagram, indicating the eutectic composition and temperature*

four stages. First stage is used to outgas the absorbant, and aligned wafers are heated up to above 150 °C. In the next step, the spacers are removed and the wafers are put into contact. Moreover, the temperature arises in this step in order to activate the getter. Then, the temperature is increased to 20-30 degrees above the eutectic point. The eutectic composition is formed thanks to the diffusion of the alloys. The temperature is held in this step for some minutes to obtain a homogeneous composition through the bonding ring. At last, the wafers are cooled down to the initial temperature to solidify the bonding layer. In the Figure 2.10, the microstructure of eutectic Al-Ge bonding, which is made on germanium dendrites within the aluminium matrix, is shown.

2.3.3.3 Transient Liquid Phase (TLP) Bonding

TLP bonding creates a metallurgical seal by forming a thin liquid phase of one low melting component in the intermediate layer system. The liquid wets the other metallic part of the bonding, later it solidifies and creates

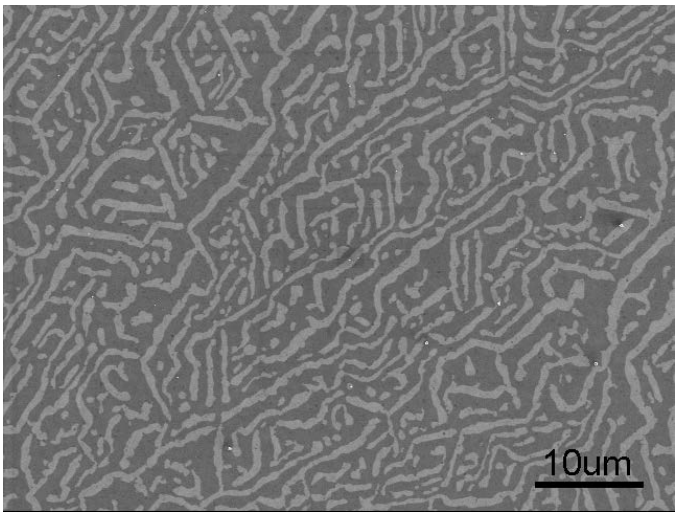

Figure 2.10: *Microstructure of Al-Ge eutectic bonding [20]*

a chemical bond through intermetallic compounds (IMCs) with the other joining metal. The advantage of this method is to obtain a fully hermetic bonding with a wide choice of material selection. The second advantage is the higher melting point of IMCs with respect to the bonding temperature, enabling multi-stack bonding without the concern about the previous ones. In TLP bonding, first the aligned wafers are taken to the chamber and the force is applied at an elevated temperature between 100-150 °C. At this stage the IMCs are formed and start to grow, due to solid state diffusion. Then, the temperature is increased to the bonding temperature, which exceeds the melting point of the material with lower T_m, typically tin or indium. The melted metal wets the surface and compensates the surface topographies and the solution of joining metal in the low melting point starts. These methods have to be used to prevent oxidization of tin or indium during bonding, while the native oxide can be avoided. The IMCs continue to grow and homogenize. Then, the cooling step completes the bonding process.
An overpressure during the bonding or a high thickness of the bonding layer may cause overflow. Hence, thickness controlling is a critical issue in this method. To do that, the intermediate layer can be deposited on one wafer, but in this way one loses the compensating topography property of this method. Also, there are several parameters that determine the thickness of the high melting point material during metallization [21, 22]:

- thickness of low melting point material;

- target bond microstructure;
- kinetics of IMCs formation;
- morphology of the growing IMCs;
- other process parameters, such as bonding temperature, time, and pressure.

The common material systems used in TLP are: i) Au-Sn with chemical composition of 17-50% Sn, resulting in the formation of $Au_5Sn(\xi)$+$AuSn(\delta)$ IMCs with remelting point of 278 °C, ii) Cu-Sn with 45% Sn composed of $Cu_3Sn(\epsilon)$+$Cu_6Sn_5(\eta)$ (415 °C) (Figure 2.11). TLP bonding has a high microstructural stability under consequent manufacturing steps and a higher mechanical strength with respect to the soldering method, due to the presence of the intermetallic compounds.

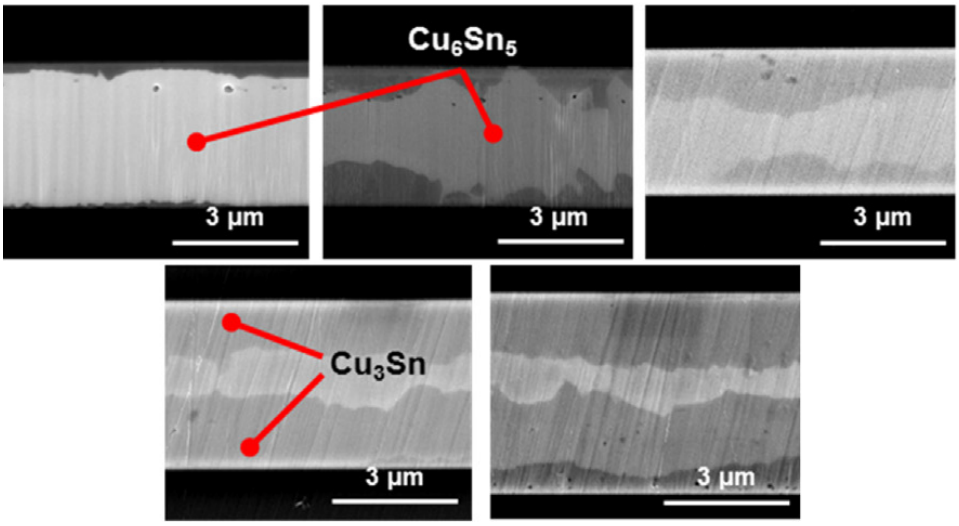

Figure 2.11: *IMCs in the Cu-Sn system [23]*

2.3.3.4 Thermocompression Bonding

Thermocompression bonding forms a solid-state metallurgical bond between two metals, such as Au-Au or Cu-Cu, without formation of any liquid phase. The Cu-Cu bonding is more with the purpose of creating a three dimensional stack for integrated circuits (IC) and MEMS manufacturing, while the conductivity of the copper allows the vertical integration of the device. One of the characteristics of this method is the need of a high

mechanical pressure to achieve a good bond yield, because of the lack of a melting phase. Hence, the surface condition and the bonding force as well as the residual stress in the copper layer due to CTE mismatch are the effecting factors in the quality of the bonding [24]. Tofteberg et al. [25] have investigated Au-Au bonding. They reported that the strength of the bonding does not depend on the width of bond frame, while the fracture force increases 99% when the bonding temperature exceeds 450 °C. In order to decrease the bonding force and the temperature in Cu-Cu bonding, Panigrahi et al. [26] demonstrated that, by sandwitching the copper between two titanium thin layers, the bonding can be done at 175 °C and 2.5 bar pressure. There are attempts for thermocompression bonding at room temperature. Kon et al. [27] reported that in a Ag-Au system with 70-80% Ag, the recrystallization and propagation is occurring in air, without heating the substrate. As depicted in Figure 2.12, due to the fact that the recrystallization happened at the original surface, the bonding shows almost no interface between the films.

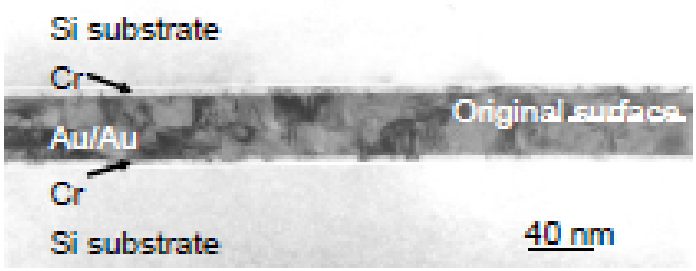

Figure 2.12: *TEM image of room temperature Ag-Au thermocompression bonding microstructure [27]*

2.3.4 Glass Frit Bonding

Glass frit bonding is a widely used method for the encapsulation of the microsystems, using a low melting point glass, and providing the advantage of an outstanding hermetic sealing and, high bonding strength. The bonding process consists of glass paste screen printing, thermal conditioning and thermocompressive bonding.
The most common glass used in this method is lead or lead-silicate glass, which has a melting point below 450 °C. The glass is deposited on the cap wafer by viscous flow during screen printing. Due to the fact that the process is rough and there is a mechanical contact of the screen mesh, the less sensitive wafer, that is the cap, is chosen for glass frit deposition. In

the screen printing, first a thin photoresist layer is deposited on the mesh to define the frame of the bonding, known as glue lines. Then, a squeegee spread the viscose glass frit on the inclined mesh (see Figure 2.13), over the predefined glue lines. One of the advantages of screen printing is that there is no need of other complementary processes such as lithography or etching for glass frit deposition. To ensure hermetic bonding and to prevent the

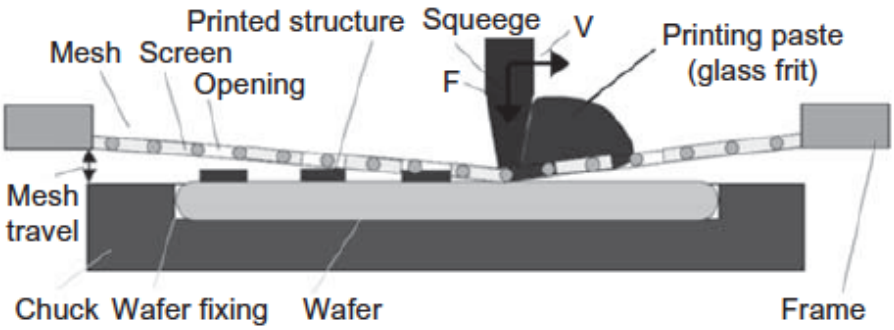

Figure 2.13: *Screen printing of glass frit on the cap wafer*

interception of the glue line and structural parts of the microsystems, there are minimum values for the width and spacing between glue lines, which have to be respected during screen printing, Yifang et al. reported a method using two-step wet etching to control the height of the glass frit layer [28]. Chen et al. [29] introduced a new method called barrier trench technology (BTT), in which the glass frit is constrained by a trench that prevents glass frit from further expansion induced by bonding process load (Figure 2.14). For the next step, thermal conditioning is applied on the paste, in order to transform into glass (Figure 2.15). First, the paste is heated up to 120 °C, then it is dried and the binder makes it stable by polymerization. In the following, the temperature rises to 340 °C to outgas the film and, as the final stage, the temperature reaches the melting point to achieve a compact and inclusion-free glass frit film. The other method for glass frit bonding is presented by Kind et al. [30], utilizing laser beam. While the glass frit is deposited on the substrate, the laser beam which passes through a transparent glass wafer as a above layer, inducing sealing process by optical to thermal energy conversion on glass frit. They also reported that a preheat up to 100 °C allows to increase the scan velocity up to 20 mm/min.
The bonding principle in glass frit bonding is the temperature rise to 425-450 °C, when the viscosity of the glass is low and, due to the presence of a mechanical force, the film wets the other wafers. During the cooling phase, a hermetic strong bond is formed thanks to the atomic diffusion. The

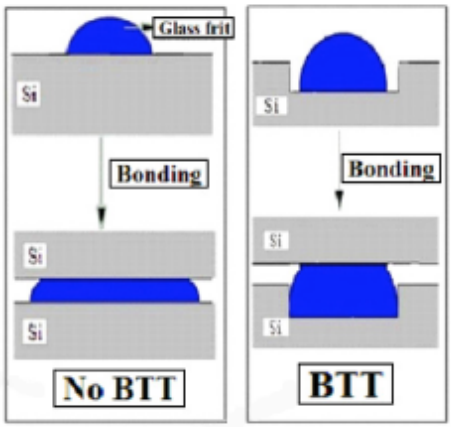

Figure 2.14: *Glass frit bonding configuration in BTT method [29]*

bonding temperature is the critical parameter, as it guarantees the sufficient wetting of the glass frit on the surface of the bonding wafer, while it does not have to be so high that the glass frit flows over the structural part of the device.

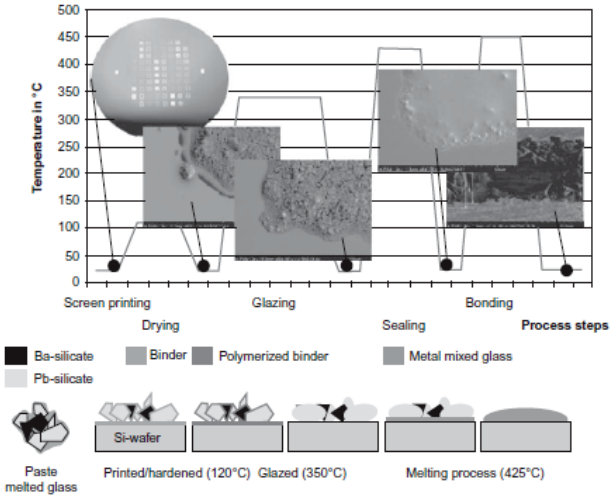

Figure 2.15: *Thermal conditioning of glass frit paste into the glass [6]*

Since there is a thermal expansion coefficient mismatch between silicon and

glass frit, there is warpage in the wafers, as reported in [31]. Consequently, a residual stress is formed after the glass frit bonding process. For more details, the effect of glass frit on the silicon substrate and, generally, the warpage (see Figure 2.16) and the residual stress resulting from thin film deposition are discussed in the next Chapters.

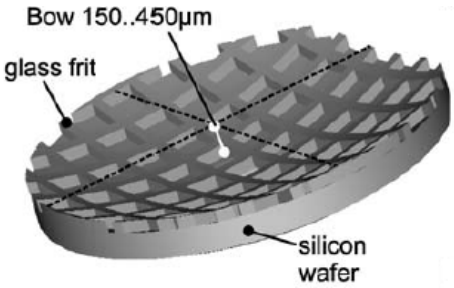

Figure 2.16: *Warpage in silicon substrate after glass frit bonding [31]*

CHAPTER 3

The Stoney Formula and its Application

3.1 Introduction

In 1909, Stoney observed that a copper electrodeposited layer was peeled off from silver substrate, if the thickness of the copper layer exceeded a certain value. He recognized that the substrate under a thin film is in a state of tension or compression without any external loads. The strain applied to the substrate leads to its bending. Stoney introduced a simple formula by which the curvature of the substrate can be calculated [32]. In the following Sections, first the derivation of the Stoney formula and, then, its application in the thermocompressive bonding will be discussed.

3.2 The Stoney Formula

Let us suppose that on a circular disk shape substrate with a uniform thickness of h_s and the radius of R, where $R >> h_s$, a thin film with the thickness of h_f is bonded. In a cylindrical coordinate system (r, θ, z), the midplane of the substrate passes through the origin of the z-axis (Figure 3.1). The film has an incompatible mismatch strain, which could be coming from thermal expansion, epitaxial mismatch or phase transformation.

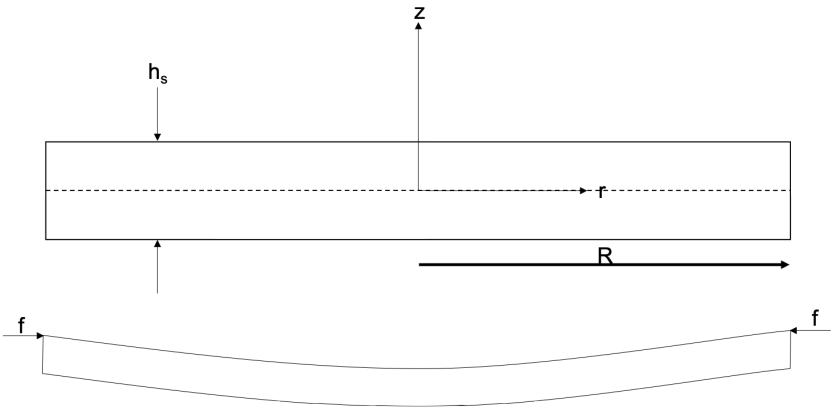

Figure 3.1: *Free system curvature of substrate due to strain mismatch (Upper: the substrate in free tension state; lower: the substrate deformation under the effect of thin film)*

The materials are assumed isotropic elastic, where the Young's modulus and the Poisson's ratio of the substrate are E_s and ν_s, respectively. By ideally separating the film from the substrate, an external force is applied on the substrate and the film tension is relaxed (see Figure 3.1). To investigate the deformation of the substrate, some assumptions are made.

- The substrate deforms according to the Kirchhoff hypothesis in the thin plate theory, with $\sigma_z = 0$ everywhere, so that ϵ_{rz} and $\epsilon_{\theta z}$ are also zero.
- All the components of the displacement gradient are very small compared to unity, thus the linear theory of elasticity can be applied.
- The contribution of the film to the overall elastic stiffness is neglected.
- The membrane force f in the film is the only parameter determined by the strain mismatch, provided that the membrane force change due to the deformation of the substrate is small compared to f.

Moreover, there are other assumptions focusing on the deformation:

- the deformation is axial symmetric and all fields are independent of θ;
- the curvature of the midplane is spatially uniform;
- the in-plane strain at the midplain is uniform, so $\epsilon_{rr}(r, 0) = \epsilon_{\theta\theta}(r, 0) = \epsilon_0$;

- localized edge effects, where the load transfers between film and substrate, can be ignored.

The strain energy density at the substrate is:

$$U(r,z) = \frac{\mu_s}{1-\nu_s}[\epsilon_{rr}^2 + \epsilon_{\theta\theta}^2 + 2\nu_s\epsilon_{rr}\epsilon_{\theta\theta}] \tag{3.1}$$

μ_s being the elastic shear modulus: $\mu_s = \frac{1}{2}\frac{E_s}{(1+\nu_s)}$. For small deformations, the strains can be expressed by radial and out-of-plane displacement in the middle plane, $u(r)$ and $w(r)$ respectively:

$$\begin{aligned} \epsilon_{rr}(r,z) &= u'(r) - zw''(r) \\ \epsilon_{\theta\theta}(r,z) &= \frac{1}{r}u(r) - \frac{z}{r}w'(r) \end{aligned} \tag{3.2}$$

In this equation, the prime indicates differentiation with respect to the argument. For small deflections, the radial and out-of-plane displacements are uncoupled. For the midplane:

$$u(r) = \epsilon_0 r \qquad w(r) = \frac{1}{2}\kappa r^2 \tag{3.3}$$

where κ is the curvature of the midplane. Due to the symmetry and translational invariance, the final shape of the midplane is spherical; considering the isotropic behavior and the small deformation, this hypothesis is a good approximation. Because in the substrate there is an equi-biaxial strain, the constitutive behavior can be represented by a biaxial elastic modulus. In an isotropic elastic material, the biaxial elastic modulus, M_s, is defined as:

$$M_s = E_s/(1-\nu_s) \tag{3.4}$$

So, the strain energy density becomes:

$$U(r,z) = M_s(\epsilon_0 - \kappa z)^2 \tag{3.5}$$

The total potential energy can be calculated as follows:

$$V(\epsilon_0,\kappa) = 2\pi\int_0^R\int_{-h_s/2}^{h_s/2} U(r,z)rdzdr + 2\pi Rfu_r(R,h_s/2) \tag{3.6}$$

The equilibrium midplane deformation corresponds to a stationery potential energy with respect to variation of its arguments ($\partial V/\partial\epsilon_0 = \partial V/\partial\kappa = 0$). These equations lead to calculation of curvature:

$$\kappa = \frac{6f}{M_s h_s^2} \tag{3.7}$$

The secondary result is the neutral plane in the substrate, which is:

$$z_{np} = \frac{\epsilon_0}{\kappa} = -\frac{1}{6}h_s \tag{3.8}$$

3.3 The Stoney Formula on glass frit film deposition

This Section is dedicated to apply the Stoney formula to the system consisting of a silicon wafer substrate and a glass frit layer as a thin film. By replacing the properties of silicon and glass frit, presented by Table 3.1, into the Stoney formula 3.7, if the temperature decreases from 440 °C to room temperature (25 °C), the curvature is obtained:

Material property	Value
Silicon	
E	169 GPa
ν	0.23
α	$2.3\times10^{-6}\ ^\circ C^{-1}$
thickness	525 μm
Glass frit	
E	85 GPa
ν	0.3
α	$7.0\times10^{-6}\ ^\circ C^{-1}$
thickness	20 μm

Table 3.1: *Material properties of substrate and thin film*

$$\begin{aligned} \epsilon_{thermal} =& (\alpha_f - \alpha_s)\Delta T = 1.95 \times 10^{-3} \\ \sigma_m =& \epsilon_m M_f = 236.8\,\text{MPa} \\ \kappa =& \frac{6f}{M_s h_s^2} = \frac{6\sigma_m h_f}{M_s h_s^2} = 4.69 \times 10^{-4} mm^{-1} \end{aligned} \tag{3.9}$$

The curvature value obtained from the 4-inch silicon wafer bonded with glass frit is obtained 3.02×10^{-5} mm^{-1}. There are several reasons behind this difference. First, the assumption of isotropic elasticity in Stoney formula; while the silicon is anisotropic. Moreover, in the bonding process, there is a mechanical pressure applied to the wafers that is not considered in the external forces applied to the substrate. Finally, the different layer configuration of wafer-to-wafer bonding with respect to the substrate-thin film configuration leads to different curvatures. Therefore, to observe the effect of glass frit on the warpage of bonded silicon wafers, Stoney formula is not

sufficient to take into account for the implied residual stresses by glass frit to silicon wafers.

3.4 Effect of Film Thickness

Freund et al. [33] discussed the effect of the thickness of the film on the curvature. The film experiences an elastic strain, causing a stress equal to $\sigma_m = M_f \epsilon_m$. At the first state (see Figure 3.1), there is no interaction between the film and the substrate, then the artificially applied traction is relaxed. The result is a deformed configuration associating to a strain energy, different with respect to the Stoney formula case:

$$U(r,z) = \begin{cases} M_s(\epsilon_0 - \kappa z)^2, & -1/2h_s < z < 1/2h_s \\ M_f(\epsilon_0 - \kappa z + \epsilon_m)^2, & 1/2h_s < z < 1/2h_s + h_f \end{cases} \tag{3.10}$$

By calculating the total strain energy, the curvature and the extensional strain of the midplane is obtained by $\partial V/\partial\epsilon_0 = \partial V/\partial\kappa = 0$,

$$\frac{\kappa}{\kappa_{St}} = (1+\frac{h_f}{h_s})[1+4\frac{h_f}{h_s}\frac{M_f}{M_s}+6\frac{h_f^2}{h_s^2}\frac{M_f}{M_s}+4\frac{h_f^3}{h_s^3}\frac{M_f}{M_s}+\frac{h_f^4}{h_s^4}\frac{M_f}{M_s}]^{-1} \tag{3.11}$$

$$\frac{\epsilon_0}{\epsilon_{0,St}} = (1+\frac{h_f^3}{h_s^3}\frac{M_f}{M_s})[1+4\frac{h_f}{h_s}\frac{M_f}{M_s}+6\frac{h_f^2}{h_s^2}\frac{M_f}{M_s}+4\frac{h_f^3}{h_s^3}\frac{M_f}{M_s}+\frac{h_f^4}{h_s^4}\frac{M_f}{M_s}]^{-1} \tag{3.12}$$

where

$$\kappa_{St} = \frac{6\epsilon_m}{h_s}\frac{h_f}{h_s}\frac{M_f}{M_s} \qquad \text{and} \qquad \epsilon_{0,St} = -\epsilon_m\frac{h_f}{h_s}\frac{M_f}{M_s} \tag{3.13}$$

Deviation from unity on the right side of the Equations 3.11 and 3.12 demonstrate the effect of the film thickness. The value obtained for κ in Stoney formula is the limiting case of Equation 3.13, where $h_f/h_s \to 0$. As reported in [34], two approaches are considered, in order to study the effect of the h_f/h_s on substrate curvature. First, is a series expansion in powers of h_f/h_s, for any value of the ratio between the biaxial moduli. In this case the curvature is:

$$\kappa \approx \frac{6\epsilon_m}{h_s}\frac{M_f}{M_s}\frac{h_f}{h_s}\left[1+\left(\frac{M_s-4M_f}{M_s}\right)\frac{h_f}{h_s}\right] \tag{3.14}$$

A second way to consider the effect of the film thickness is to establish a range for the values corresponding to h_f/h_s and M_f/M_s, where the error occurs in the using of Stoney formula is less than a certain value:

$$\left|\frac{\kappa h_s}{6\epsilon_m}\frac{h_s}{h_f}\frac{M_s}{M_f} - 1\right| \leq \text{Certain error value} \tag{3.15}$$

In the case of glass frit deposition on the silicon wafer, the effect of the thin film shrinkage on the substrate curvature is reported in Figure 3.2, based on Equation 3.14. However, because of the aforementioned differences with

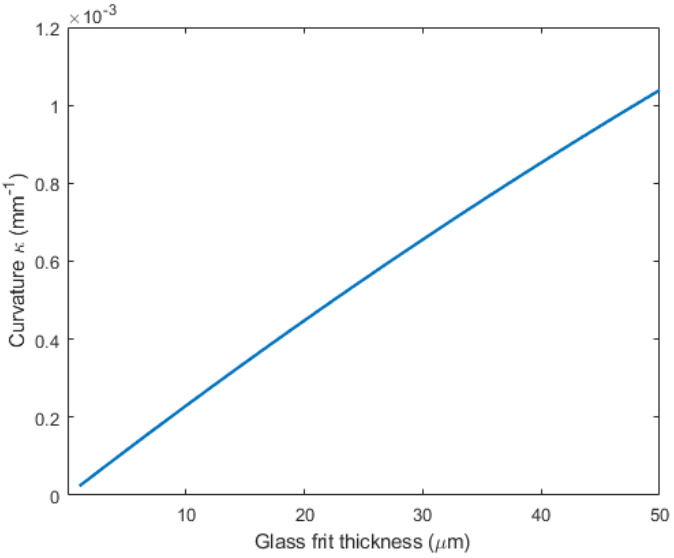

Figure 3.2: *Effect of glass frit substrate on the curvature of the silicon wafer.*

respect to the silicon wafer configuration adopted in the industrial context, this result has be considered only as indicative and more accurate numerical simulations are carried out in the following of the thesis.

CHAPTER 4

Material Characterization

4.1 Introduction

In order to model the bonding process, it is necessary to know the properties of the materials in the system and the experimental test carried out to interpret their behavior. Hence, in this Chapter the properties of the glass frit will be discussed. First, the surface topography of the glass frit is studied. Then, the mechanical properties obtained from nanoindentation tests and the procedure to obtain parameters from the curves are described. Finally, the microstructure characteristics acquired by scanning electron microscopy as well as the chemical composition will be presented.
In the literature, there are few attempts to study the glass frit experimentally. For instance, Dresbach et al. [35] investigated the bonding strength via micro chevron test. The fracture toughness obtained for glass frit is 0.57 MPa$\sqrt{m}$. However, it is necessary to investigate experimentally to obtain other properties of glass frit.
Figure 4.1 shows the glass frit deposited on silicon wafer and glass frit bonded dies, which are used in the sets of experiments discussed in this Chapter.

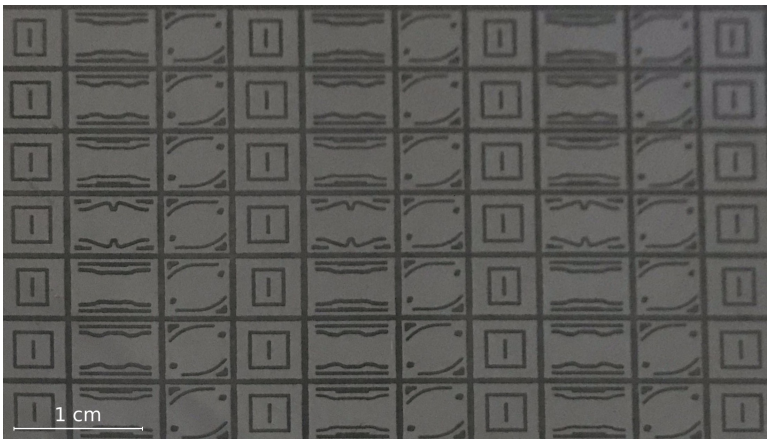

Figure 4.1: *Glass frit pattern on silicon wafer*

4.2 Laser Profilometry

As one of the main factors affecting the bonding yield and quality is the surface topology, the surface roughness of the glass frit has been measured with laser profilometry. First, in order to describe the surface texture quantitatively, the definition of the parameters is presented [36].

Definition 4.2.1. *Arithmetic average height (R_a): the average absolute deviation of the roughness irregularities from the mean line over one sampling length.*

$$R_a = \frac{1}{l}\int_0^l |y(x)|dx$$
$$or\ R_a = \frac{1}{n}\sum_{i=1}^{n}|y_i|$$

where l is the length of scan; $|y(x)|$ is the out of plane position of the point with respect to the reference plane; and n is the number of the points on which the topography measurement is happening.

Definition 4.2.2. *Root mean square roughness (R_q): standard deviation of*

the distribution of surface heights.

$$R_q = \sqrt{\frac{1}{l}\int_0^l y(x)^2 dx}$$

$$or\ R_q = \sqrt{\frac{1}{n}\sum_{i=1}^{n} y_i^2}$$

Definition 4.2.3. *Maximum height of peaks (R_p): maximum height of the profile above the mean line within the assessment length.*

Definition 4.2.4. *Maximum depth of valleys (R_v): defined as the maximum depth of the profile below the mean line within the assessment length.*

Definition 4.2.5. *Maximum height of the profile (R_t): vertical distance between the highest peak and the lowest valley along the assessment length of the profile.*

The working principle of the ray profilometry is based on an infrared light from a semiconductor laser focused to a spot by an objective lens. The light is reflected from the sample being measured and directed by a beam splitters with a prism. The light beam is reflected on photodiodes as pair of spots. Both diodes are illuminated equally unless the distance between the objective lens and the surface is different with respect to the focal length of the lens. This generates a signal to the control circuit. Then, the objective lens is dynamically repositioned until the correct focus distance is adjusted. The movement of the objective lens represents the surface profile.

4.2.1 Results

An exemplary surface profile of the deposited glass frit is reported in the Figures 4.2 and 4.3, which show the results along and across the glass frit layer, respectively. The surface of the glass frit is not as smooth as the wafers, therefore in this method the contact points of the binder and the sensor wafer are not as many as in the direct bonding; however, due to the fact that the glass is partially melted at the bonding temperature, it wets the wafer sufficiently.

Another analysis performed by exploiting the laser profilometry concerns the cross section of the silicon die. The results of this test confirm the supplementary shrinkage of glass frit with respect to the silicon (see Figure 4.4). The roughness results of the glass frit layer are reported in Table 4.1.

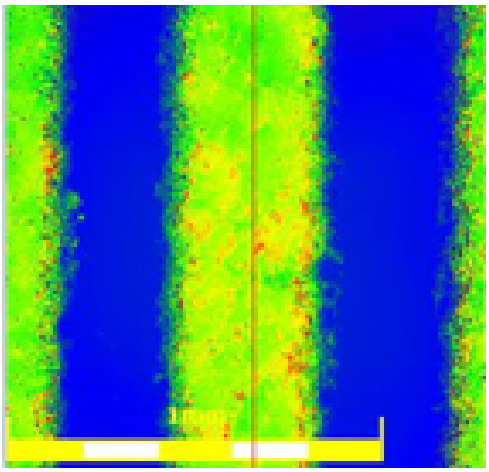

(a) *Laser profilometry path*

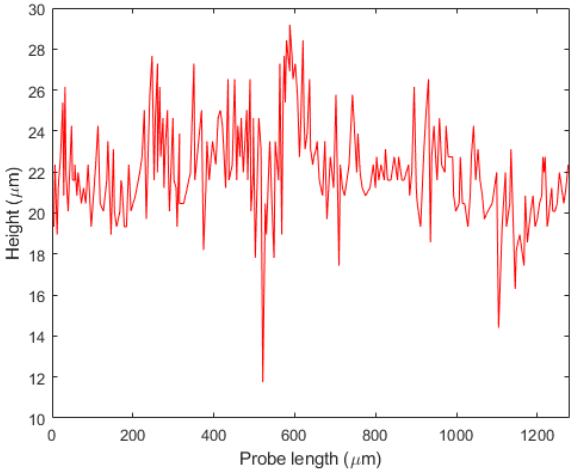

(b) *Surface roughness profile of the glass frit*

Figure 4.2: *Glass frit laser profilometry results along the glass frit layer*

Parameter	Value
R_t	20.136 μm
R_a	1.585 μm
R_q	2.168 μm
R_p	7.866 μm
R_v	12.270 μm

Table 4.1: *Roughness parameters of the glass frit layer*

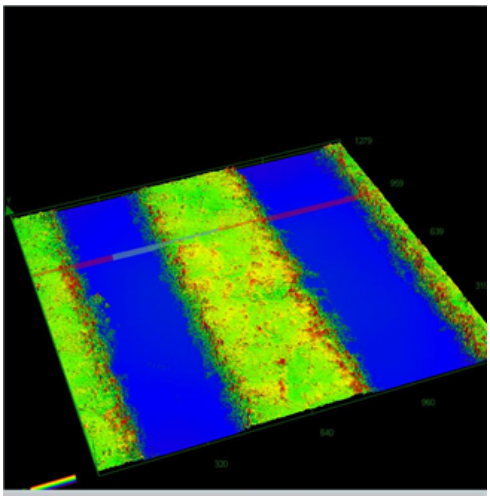

(a) *Laser profilometry path*

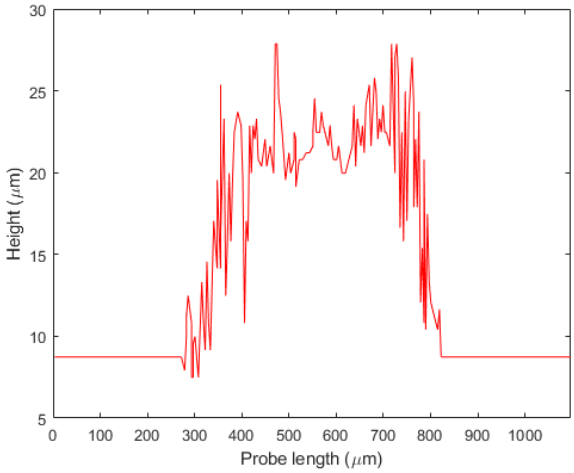

(b) *Surface roughness profile of the glass frit*

Figure 4.3: *Glass frit laser profilometry results across the glass frit layer*

4.3 Nanoindentation Test

By nanoindentation test, hardness and elastic modulus properties can be obtained through load-displacement curves without taking a picture of the indentation, which is a mandatory part of the evaluation in macroindentation. Also, the fracture toughness can be measured in ultra-thin films [37]. The material used as indenter is diamond, due to high hardness and elastic modulus, minimizing the indenter effect on the measurement of the film's

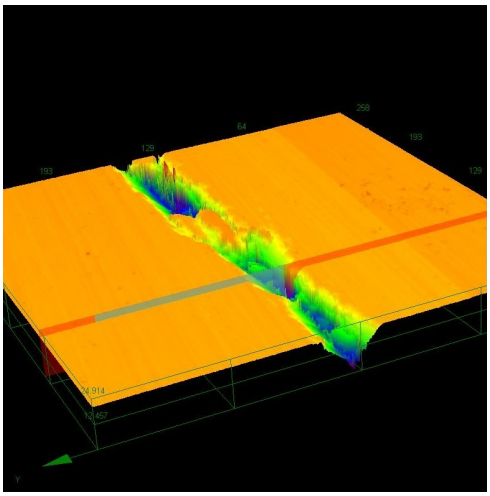

(a) *3D surface profilometry results for the silicon-glass frit-silicon section*

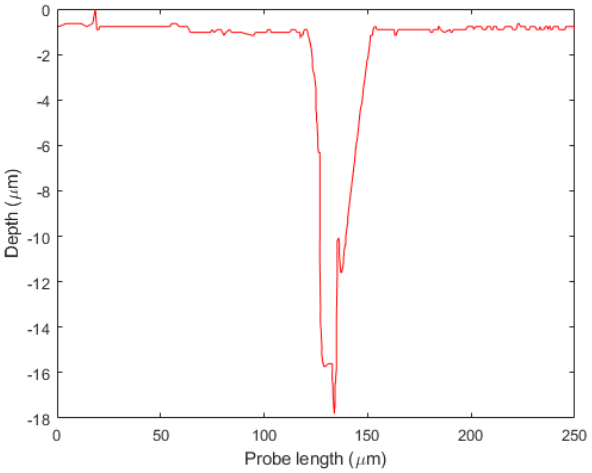

(b) *Linear profilometry results*

Figure 4.4: *Glass frit shrinkage due to the higher thermal expansion coefficient*

mechanical properties. Besides, the indenter chosen shape is the Berkovich triangular pyramid, hence it is easily ground to sharp points. Also, in order to determine the mechanical properties of a thin film and remove the effect of the substrate, the indentation depth must be less than 10% of the film thickness [38].

Figure 4.5 demonstrates the typical load-displacement curve of a nanoindentation test. To measure the hardness, the indentation load peak is divided

by the projection of contact area.

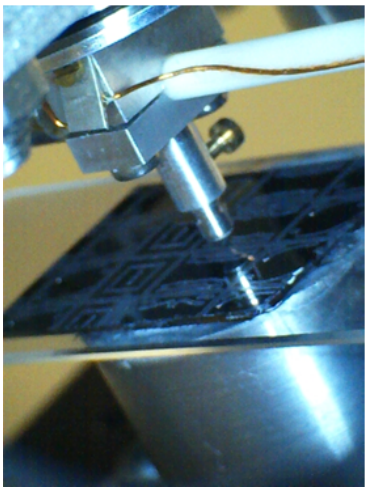

(a) *Indentation test setup*

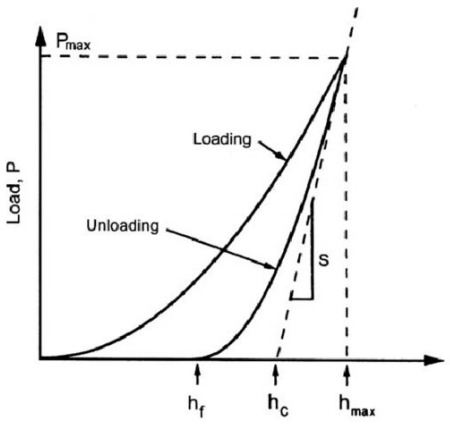

(b) *Indentation curve for indentation test*

Figure 4.5: *Indentation test setup and its typical result curve*

$$H = \frac{P_{max}}{A} \tag{4.1}$$

The elastic modulus can be obtained by the initial unloading contact stiffness, $S = \frac{dP}{dH}$. Also, based on the relationships developed by Sneddon [39], a geometry-independent relationship involving contact stiffness, contact area, and elastic modulus can be derived as follows:

$$S = 2\beta\sqrt{\frac{A}{\pi}}E_r \tag{4.2}$$

where β is a constant depending on the shape of the indenter (β=1.034 for Berkovich), and E_r is the reduced modulus, based on the fact that the deformation occurs both on the sample and the indenter. E_r can be calculated as below:

$$E_r = \frac{1-\nu^2}{E} + \frac{1-\nu_i^2}{E_i} \tag{4.3}$$

where ν and E are the Poisson's ratio and Young's modulus of the sample and ν_i and E_i are the same parameters for the indenter. In order to calculate the glass frit elastic modulus from Equations 4.2 and 4.3, the contact stiffness and the projected contact area should be obtained from the load-displacement curve. The non-linear unloading curve can be described as a

power law, based on Doerner and Nix suggestion [40]:

$$P = B(h - h_f)^m \tag{4.4}$$

where h_f is the final displacement after complete unloading, B and m are fitting parameters. The parameters B and m for this test are obtained as $2.1\times10^{-4}\pm1.59\times10^{-4}$ and 2.08 ± 0.25, respectively. The unloading stiffness is obtained by differentiating of Equation 4.4 with respect to h at $h = h_{max}$.

$$S = \left(\frac{dP}{dh}\right)_{h=h_{max}} = Bm(h - h_f)^{m-1} \tag{4.5}$$

The projected contact area for a known indenter can be calculated from the contact depth h_c, namely in the case of Berkovich indenter:

$$A_c = 24.56\, h_c^2 \tag{4.6}$$

As the indenter is not ideally sharp, calibration of the area function is necessary [41].

4.3.1 Experimental Results

In order to measure the mechanical properties of glass frit via nanoindentation, the samples are divided to two groups, the first one obtained from the tests at the center of the wafer (hereafter known as sample A), and the second one from tests at the edge (hereafter known as sample B). Within these two main groups, a test series is performed on the solid glue lines and the cross sections. In this way, the effect of the position as well as the topology

Parameter	Value
Maximum load	100 mN
Indenter contact velocity	0.10 μm/s
Loading rate	10.00 mN/s
Unloading rate	20.00 mN/s

Table 4.2: *Nanoindentation test conditions*

of the glass frit can be studied. The indentation test conditions are reported in Table 4.2. The other important parameter in the nanoindentation test is the surface condition. There are several studies to investigate the effect of surface roughness on the nanoindentaion results. For instance, Jiang et al. studied via finite element method the effect of roughness on the nanoindentation of the thin films [42]. Also Miller et al. studied the effect of the RMS roughness on the cement paste as a heterogeneous material [43]. However,

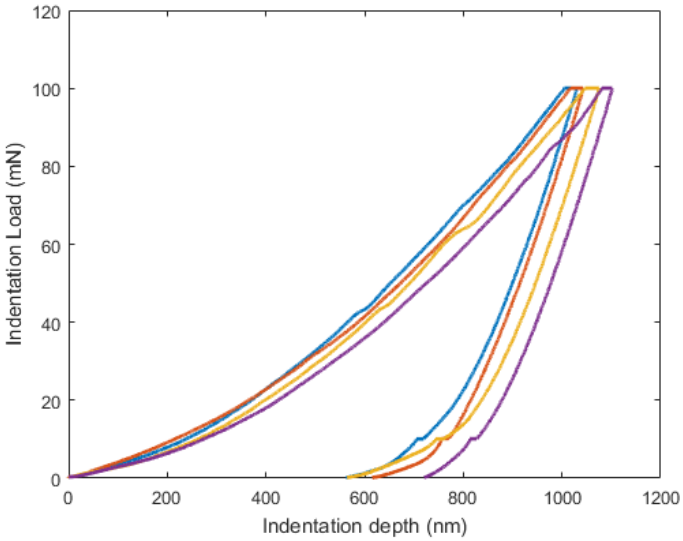

Figure 4.6: *Indentation test results*

there is a rule of thumb indicated in [44], that the thickness of the sample has to be 10 times of the indentation depth or three times of the indenter diameter. As the thickness of the glass frit is 20 μm and the indentation depth is about 1 μm (see Figure 4.6), it fulfills this rule and has the minimum criterion for the test.
The results of the nanoindentation show that the difference between the properties at the center and at the edge is negligible, hence the properties of the binder is homogeneous, regardless of the position on the wafer. Figures 4.6 and 4.7 show the results for the elastic modulus and the hardness. The elastic modulus is about 85$\pm$9 GPa, while the hardness obtained is 5.3$\pm$0.7 GPa.

4.4 Microstructure

To study in deep the properties of glass frit, microstructural analyses have been performed via scanning electron microscopy (SEM) and energy-dispersive X-ray spectroscopy (EDX). In SEM, the surface is analysed with the interaction of an electron beam with the sample. The image is produced by secondary electrons or reflected backscattered electron beam. Secondary electrons are most valuable for showing morphology and topography on samples, since they are emitted from very close to the surface and the image has a higher resolution, while the backscattered electrons, produced by

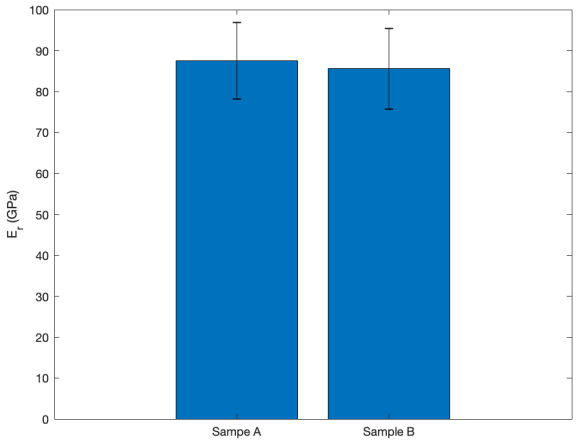

(a) *Elastic modulus*

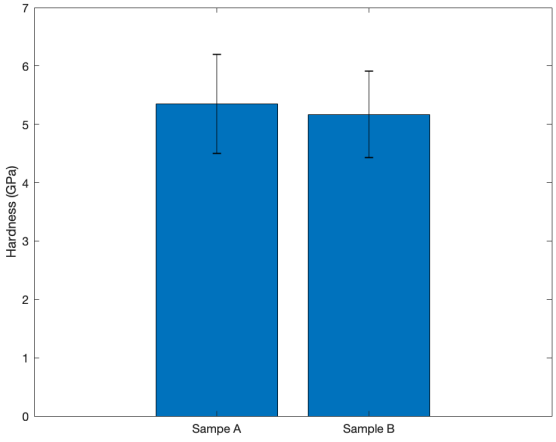

(b) *Hardness*

Figure 4.7: *Mechanical properties of glass frit*

elastic scattering, are instead coming from deeper locations in the specimen and, consequently, the image shows lower resolution. As the backscattered electrons intensity highly depends on the atomic number, it is valuable for illustrating contrasts in the composition of multiphase samples.
As mentioned in the SEM working principle, an incident electron beam can stimulate an electron in the lower-energy shell of the atom and eject it. In order to reach the steady state, an electron from a higher-energy shell sub-

stitutes the ejected one. Because of the difference in the energy levels, this energy is released in a X-ray form. Depending on the atomic number and energy difference between the energy levels, the atomic composition can be therefore studied.

4.4.1 SEM Analysis

As glass frit is an amorphous material, in order to be analyzed with SEM, first it is coated with a thin conductive Au/Pd layer. Then, the backscattered SEM analysis has been carried out on the bonded and non-bonded glass frit. The non-bonded samples can be categorized in two groups: i) deposited glass frit film on the silicon and ii) glass frit after die breakage (the results for this group is presented in the next Chapter). As depicted in Figure 4.8, the glass frit is a porous material with a homogeneous matrix. The rough surface of the film with respect to the silicon can be observed (Figure 4.8.a).

As discussed in the Chapter 3, thin film deposition on the silicon wafer can introduce warpage to the substrate. The experimental proof of the effect of glass frit deposition on silicon substrate is presented in Figure 4.9, where the transversal SEM view of the die after bonding is depicted. Exploiting an image processing software, ImageJ, the distribution of the phases in the glass frit microstructure has been measured. This software creates a binary version of photo, which keeps the phase dark and makes the rest a uniform white background, and it calculates the area and the distribution of this phase within the background. Table 4.3 shows the results of the SEM image analytic results for the 8,775 μm^2 glass frit.

Parameter	Value
Area percentage	17.32%
Total area	1,520 μm^2
Mean value	254 μm^2

Table 4.3: *SEM image analytic results*

Another outcome of the SEM and laser profilometry of a bonded silicon die is the recognition of the presence of silicon at the position of glass frit layer. This configuration comes from the fact that the wafers are cut to the dies after the bonding process. Due to high abrasion in the dicing, silicon particles from wafers misplaced in between the silicon layers, where there is a void space due to the shrinkage of the glass frit towards the inside of the die (see Figure 4.4). The SEM and laser profilometry of these silicon particles are presented in Figure 4.10.

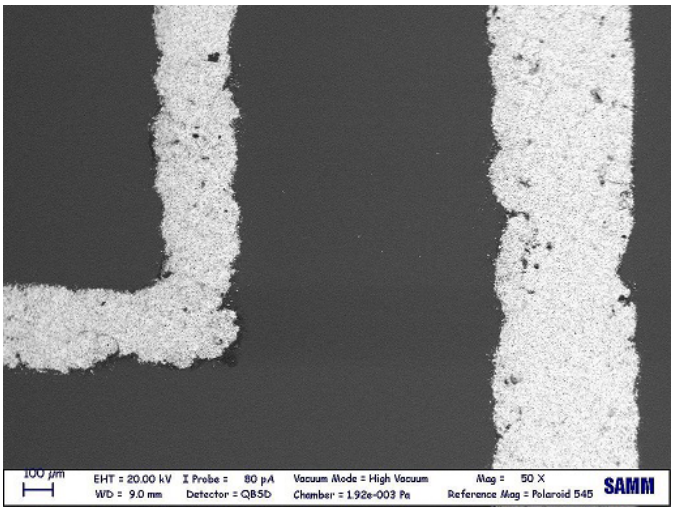

(a) *glass frit glue lines*

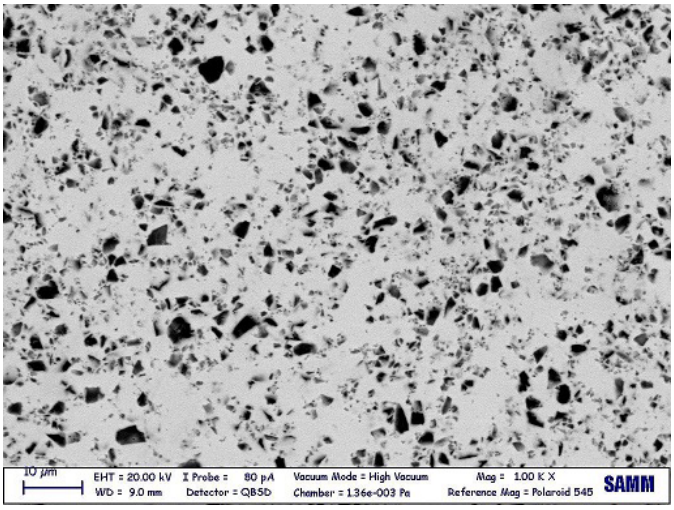

(b) *Microstructure of glass frit*

Figure 4.8: *Backscattered SEM images of glass frit*

These particles influence the mechanical reliability of the die, which will be discussed in the next Chapter.

4.4.2 Chemical Composition

By utilizing the interaction of the electron beam and the sample, the chemical composition of the sample can be also characterized. The expected composition is the presence of lead, silicon and oxygen (general lead sili-

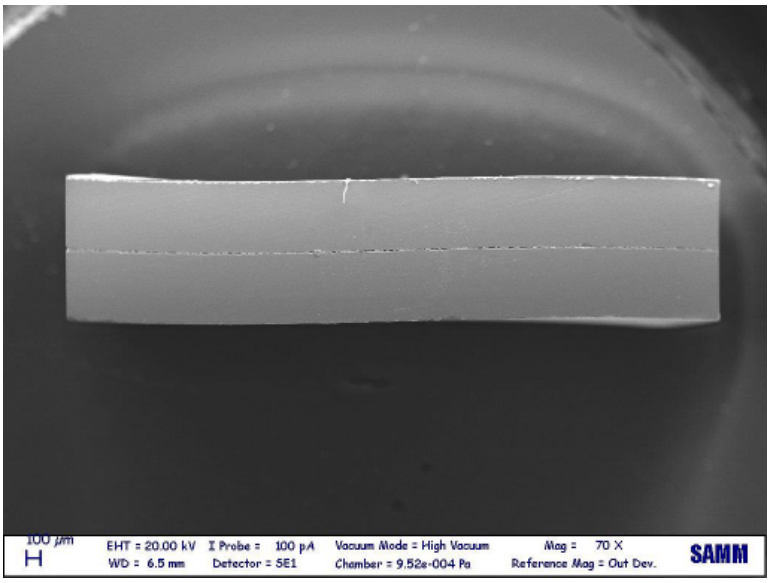

Figure 4.9: *Die warpage after glass frit bonding*

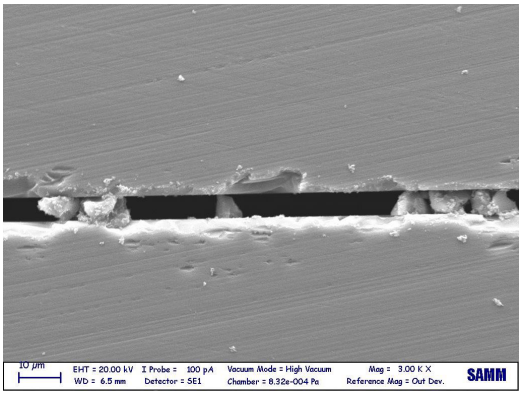

(a) *SEM image*

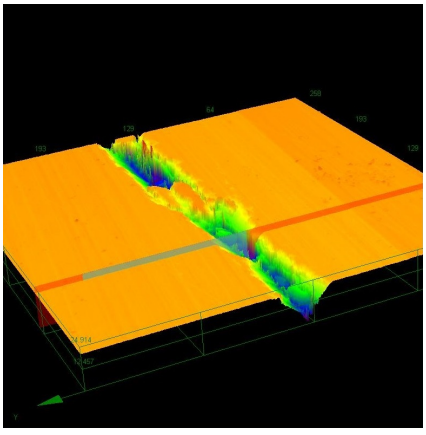

(b) *Laser profilometry*

Figure 4.10: *Experimental evidences of the presence of silicon in between of wafers after dicing*

cate glasses elements). To investigate thoroughly the composition, the microstructure is divided to dark and the bright phases, as mentioned in the Section 4.4.1. EDX analysis is done on both phases (Figure 4.11) to study the their difference, from the composition point of view. Figure 4.12 shows the results of EDX analysis and the differences between the amount of the

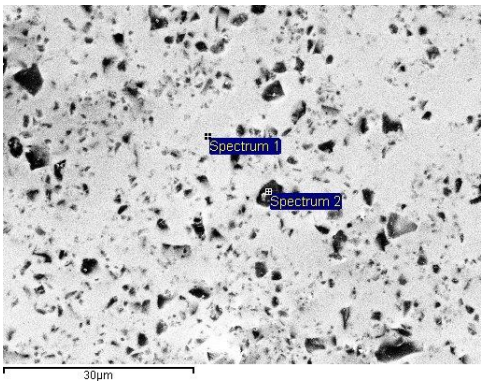

Figure 4.11: *Regions where EDX analysis is performed*

elements in each phase. The main difference between the phases is in en-

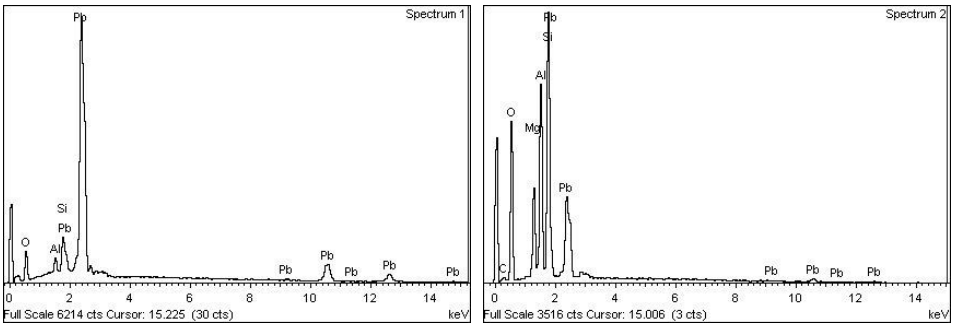

(a) *Bright phase spectrum* **(b)** *Dark phase spectrum*

Figure 4.12: *Chemical composition of glass frit obtained by EDX analysis*

richment of the dark phase in aluminium and magnesium oxide and the absence of silicon oxide with respect the bright one.
The bright phase corresponds to the glass frit matrix with presence of lead, silicon and oxygen. The dark phase relates, instead, to additives in the matrix necessary to adapt the thermal expansion coefficient to silicon. Another effect of the glass frit composition in the bonding process is the presence of the lead oxide at the interface of the silicon-glass frit, which causes diffusion of the oxygen into the silicon wafer and creates a thin silicon oxide layer at the interface, based on the Reaction 4.7:

$$\mathrm{Si} + \mathrm{PbO} \longrightarrow \mathrm{SiO_2} + \mathrm{PbO} \tag{4.7}$$

Boettge et al. shows that the presence of a thin metallic layer on the silicon wafer acts as a barrier and prevents silicon oxidation. This process also

has another benefit because it prevents lead precipitation and consequently, decreases the risk of electrical shorts [45].

CHAPTER 5

Bonding Failure Analysis

5.1 Introduction

Reliability is a concept that gains increasingly importance in any industry. Systems which are more reliable attract the target market and, consequently, rise the reputation of the product with respect to its competitors. Mechanical reliability of microsystems is not an exception. Since MEMS are employed in various industries, the comprehension of the reliability of these systems is one of the essential fields nowadays. Hsu [46] categorized the MEMS failure mechanisms into six groups:

i) mechanical failure;

ii) electromechanical breakdown;

iii) deterioration of materials;

iv) excessive intrinsic stresses;

v) improper packaging techniques;

vi) environmental effects.

In the mechanical failure, such as induced by accidental drop, the dynamic load can cause a serious damage to the package or to the structural parts of the system, as it happens to inertial MEMS for cellphones, because these devices are more exposed to this kind of event [47]. Also, thin film delamination, coming from coupled different fracture modes, is another phenomenon leading to system failure. This could occur to different levels of MEMS packaging. To evaluate this failure mechanism, fracture toughness data from a multi-layered structure is needed.
Therefore, in this Chapter the resistance of the glass frit bonded die subjected to external load is investigated experimentally and numerically. First, the results of the die shear test are presented and discussed, following by the introduction of the cohesive zone model to simulate the delamination and the die fracture.

5.2 Die Shear Test

A die shear test (see Figure 5.1) is performed to analyse the integrity of the materials attached to semiconductors or other surfaces attached to the package headers. In this method, a tool applies a uniform distributed force to the die until the rupture point, hence it is considered a destructive test. Based on the standard MIL-STD 883 method 2019.9 [48], the conditions to be respected during the test procedure are the following.

a) If the device is applying a linear load, the direction of the applying load has to be perpendicular to the die and parallel to the plane of the header or base.

b) The applying force has to gradually increase from zero to the specified value.

c) The edge of the die where the force is applied has to impose an angle equal to 90° with respect to the test stage.

d) After the contact, the relative vertical position of the tool shall not be changed.

e) The shear tool attached to the lever arm has to keep a proper distance to assure an accurate applying force.

Figure 5.2 demonstrates the minimum load versus die attach area. The 1.0x magnification of load value is the minimum strength required for the silicon die according to the standard STD-MIL883.
There are three different separation categories:

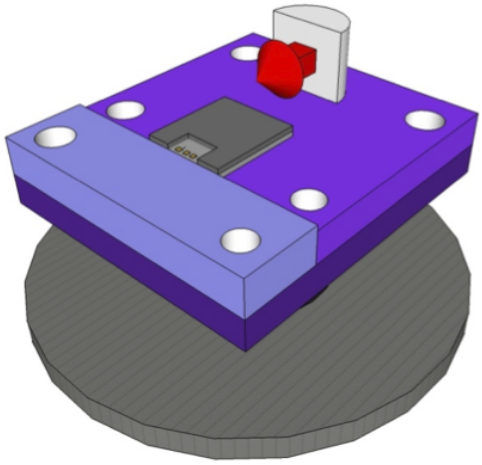

Figure 5.1: *Die shear test setup*

i) shearing of the die with residual silicon remaining;

ii) die separation from the attach medium;

iii) separation of die and attach medium from the package.

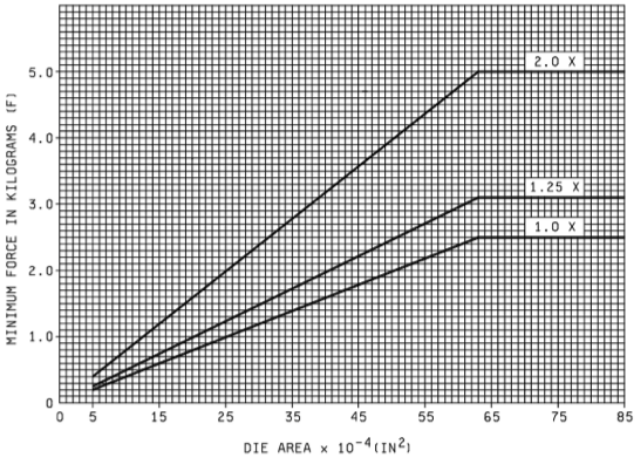

Figure 5.2: *Minimum load requirement for die failure [48]*

5.3 Setup

Die shear tests have been performed by a Condor Sigma Bonding Test machine, in which, as can be seen in Figure 5.3, there is a shear tool that imposes displacement on the side of the upper die, while the other lower half is restrained. The device is sensing the reaction force at the shear tool. In order to completely fix the lower part of the die, a stage has been designed and manufactured, as depicted in Figure 5.4. The stage has two parts attached by a screw, with the total dimension of $60\times50\times40$ mm. At the top, there is a trench with the depth 25 μm less than the the thickness of silicon substrate, hence, it prevents the movement of the lower layer and simultaneously, leaves a proper space for the movement of the upper silicon layer during the test. The materials used for stage fabrication are aluminium and steel; during the tests is confirmed that the stiffness of the stage has no significant effect on the results.

Figure 5.3: *Condor Sigma bonding test machine*

Parameters which are controlling the test are the imposed displacement, the displacement velocity and the shear height; the latter is the vertical distance between the tip of the shear tool and the stage surface at the point when the test starts. The last parameter helps to adjust the tool on the upper side of the die which is supposed to be pushed. The maximum allowable shear force is 100 kgf and the sampling rate is 2 kHz.
In order to investigate thoroughly the evolution of fracture during the test,

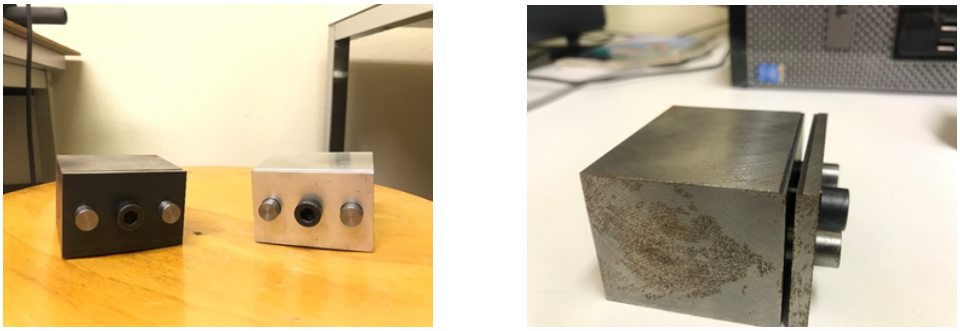

(a) *Stages made from aluminium and steel*

(b) *Trench on the stage designed for die shear test*

Figure 5.4: *Stages designed and manufactured for die shear test*

it is live captured by a Dino Lite digital microscope. Hence, for each test, the evolution of the crack and the final rupture are registered.
The parameters used for the tests, based on the configuration described above, are reported in the Table 5.1.

Parameter	Value
Shear eight	235 μm
Displacement	1.5 mm
Displacement rate	1,5,10,15 μm/s

Table 5.1: *Parameters used in the die shear tests*

5.4 Results and Discussion

The results obtained from die shear test have always been limited to the final failure load in the literature. For instance, Kim et al. [49] studied the strength of the glass frit bonding of silicon strain gauges by die shear test. Also, Sun et al. investigated the effect of surface preparation as well as process temperature on the bonding strength of glass frit soldered ceramics [50]. The effect of chemical composition on shear strength is investigated by [51] et al. which demonstrated that the addition of 15% CuO to the composition of the glass frit can increase its strength magnificently. However, there is a lack of discussion regarding to the effects of test parameters as well as failure mechanisms in the glass frit by shear test.
Hence, in this Section, first the results of the die shear test for different displacement velocity will be discussed. Then, the effect of the parameter variation on the results is investigated.

5.4.1 Load-Displacement Curves

The load-displacement curves of the die shear test can be divided into three categories. This subdivision is based on the shapes of the curve and on the evolution of the fracture in the die, as captured by the digital microscope.

Category I: pure failure in the attach medium

In this category, the crack initiates and then propagates within the glass frit layer. There is no evidence of damage in the silicon part of the die, and the glass frit remains mainly on the lower silicon part (see Figure 5.5). Figure 5.7.a shows the cracks in the glass frit film medium and 5.7.b shows the spherical lead oxide precipitates on the surface of the glass frit, after debonding by the shear test.

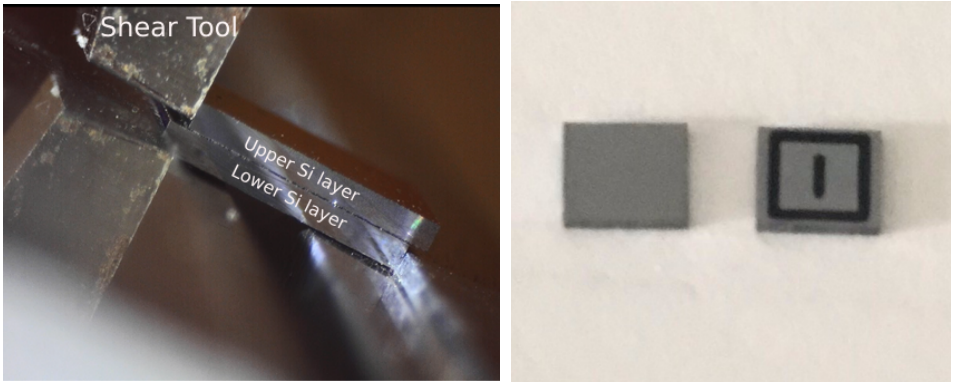

(a) *Pure shear mode failure during the test* **(b)** *Glass frit bonded die after the test*

Figure 5.5: *Failure of the glass frit bonded die in the Category I*

Figure 5.6 shows the load-displacement curve for category I.

Category II: failure in the mixed mode

In this Category, in addition to the mode II (shear) fracture mode, mode I (opening) fracture mode also plays a role in the die failure. The significant differences in this category with respect to the Category I are: first, the projectile motion of the upper silicon layer after the complete debonding, while in Category I this layer moves only in the direction of the applied force; second, the presence of the latter part of the load-displacement curve i.e. the curve zone where the slope increases in Figure 5.8. The reason

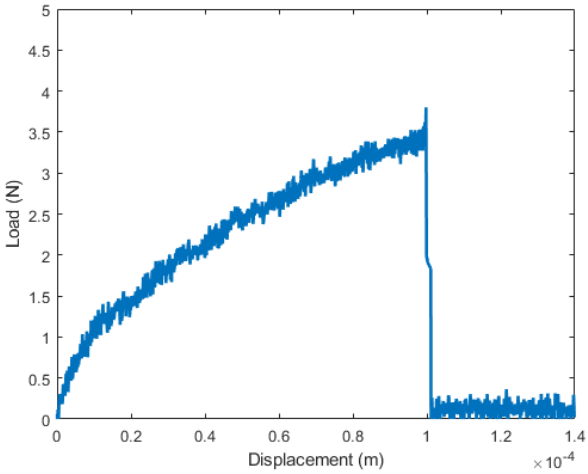

Figure 5.6: *Load-displacement curve for failure in the attach medium; displacement rate 1µm/s; category I*

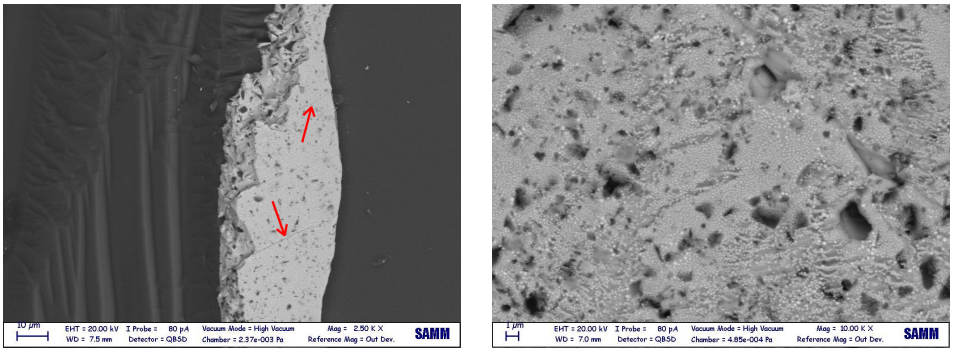

(a) *Cracks on the glass frit surface after Category I failure*

(b) *Lead oxide precipitates*

Figure 5.7: *Glass frit fracture surface*

behind this behavior is the presence of silicon debris in the interspace of silicon layers caused by the wafer dicing process (see Figure 4.10 in Section 4.4.1): this debris induces a deviation of the applied load from the purely shear direction to the normal direction of glass frit plane.

Category III: damage in silicon and die rupture

In the third Category, the crack initiates and propagates through the silicon layers. The reason is either there is a defect in the silicon layers, created

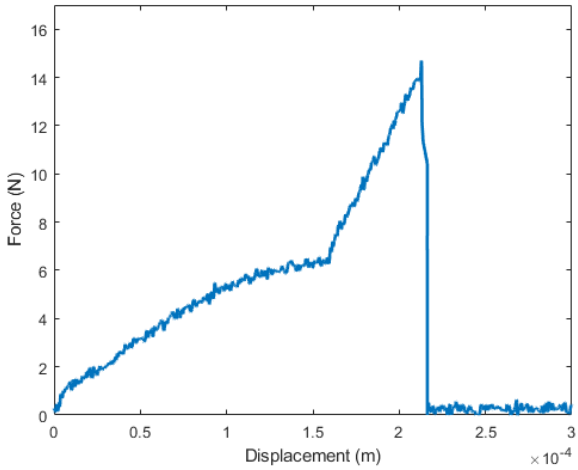

Figure 5.8: *Load-displacement curve in the rate of 15 μm/s for the mixed mode (Category II)*

in the dicing process, or it is due to the stress intensity at restrained points; hence, the crack propagates in the silicon and the die fails with a complete rupture (see Figure 5.10). As the stiffness of silicon is higher than the one of the glass frit, the failure load, as shown in Figure 5.9, is higher with respect to the two other categories.

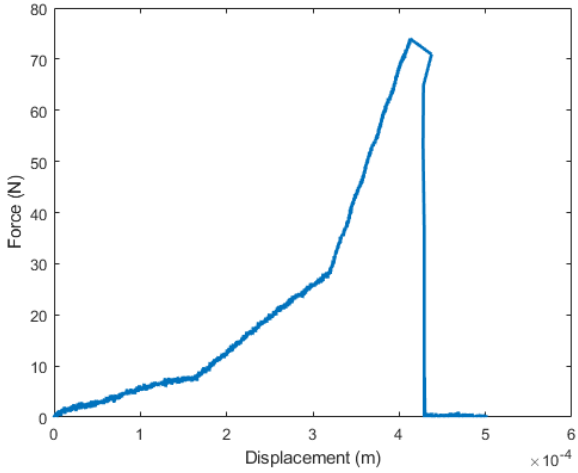

Figure 5.9: *Silicon die rupture curve (category III) in the displacement rate of 15 μm/s*

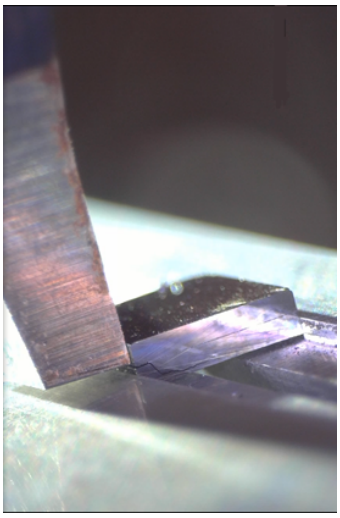

Figure 5.10: *Crack propagation in the silicon layer*

5.5 Results Overview

By comparing the results of the die shear test at different displacement rate (in the range 1-15 μm/s), it can be concluded that the higher the rate the higher the failure load. This comparison is valid if the samples fail with a similar mechanism. Figure 5.11 shows the effect of the rate on the response of the die in the all categories. The values are the mean values for each rate and mechanism. Figure 5.12 presents a summary of the all 65 die shear tests carried out in this thesis. The failure load in most cases is placed between 0-30 N (Figure 5.12.a), while the higher loads correspond to the silicon fracture phenomenon (i.e. Category III). In order to study the probability of each mechanism and its dependency to the displacement rate, the number of specimens which failed in a specific category is divided by the total number of specimens tested at the certain displacement rate. Figure 5.12.b shows the results of the probability calculation. The Category I is more likely to happen in low strain rates, while the second and the third category occurred preferentially at the elevated rates.

5.6 Numerical Analysis

5.6.1 Cohesive Zone Model

Cohesion loss and failure at the interface are debatable issues in damage mechanics. In order to model this phenomenon, there are various studies in

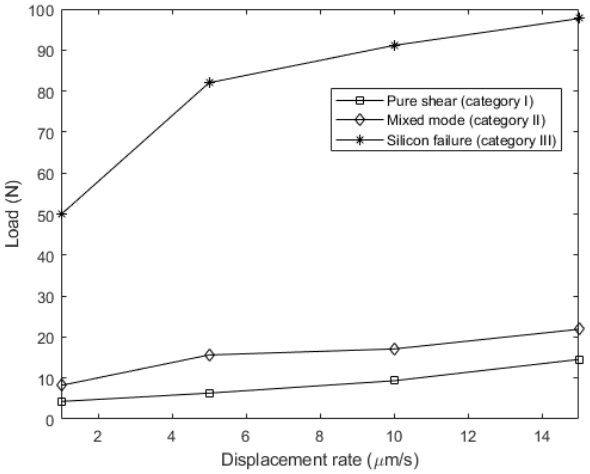

Figure 5.11: *Displacement rate dependency of failure load for each failure mechanism*

the literature based on the different applications, such as interface delamination in composites [52], fracture mechanics for concrete [53] or failure at adhesive film [54]; often these studies adopt a *cohesive zone model*. In this model, by utilizing an *interface constitutive law*, the softening and damage evolution which stems from the crack propagation can be studied.
The interface constitutive law is defined as below:

$$t = \mathcal{A}([u], x) \tag{5.1}$$

where $\mathcal{A}$ is an unspecified operator which relates to the traction vector, t, and the displacement jump, $[u]$, and x is the internal variables vector. The general class of interface laws introduced by Allix and Ladevèze [55] is described by the following set of equations:

$$[u] = [u]^e + [u]^p \tag{5.2}$$

$$\begin{aligned} E = \frac{1}{2}(1-d_1)K_1[u_1]^{e^2} + \frac{1}{2}(1-d_2)K_2[u_2]^{e^2} \\ +\frac{1}{2}(1-d_3)K_3^+ < [u_3]^e >_+^2 + \frac{1}{2}K_3^- < [u_3]^e >_-^2 + \Psi(\eta) \end{aligned} \tag{5.3}$$

$$t_i = \frac{\partial E}{\partial [u_i]^e} \qquad i = 1,2,3 \qquad Y_i = -\frac{\partial E}{\partial d_i} = 1,2,3 \qquad \chi = \frac{\partial E}{\partial \eta} \equiv h(\eta) \tag{5.4}$$

$$F = F(t_i, Y_i, \chi; d_i) \qquad G = G(t_i, Y_i, \chi; d_i) \tag{5.5}$$

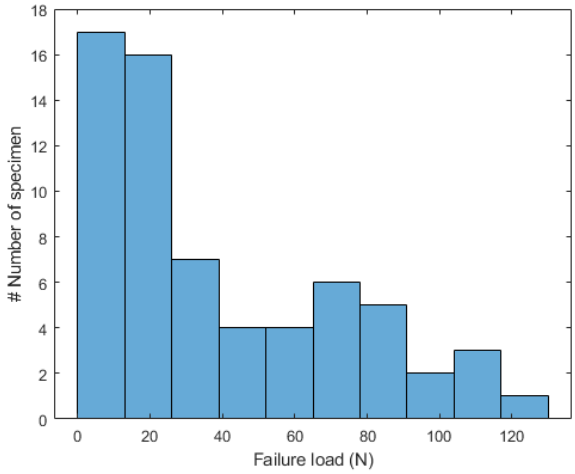

(a) *Failure load distribution*

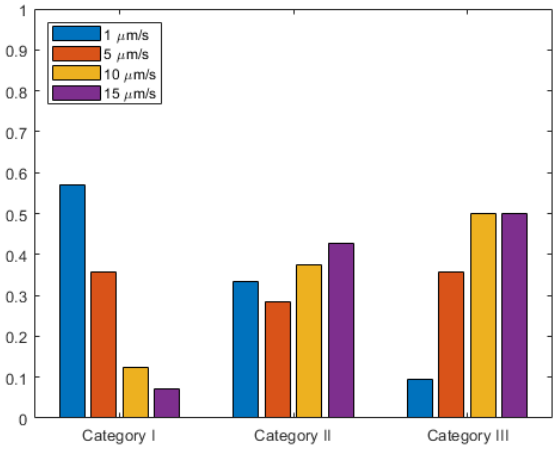

(b) *Probability of each failure mechanism for different displacement rates*

Figure 5.12: *Summary of the die shear tests*

$$[\dot{u}_i]^p = \frac{\partial G}{\partial t_i}\dot{\gamma} \qquad i = 1,2,3 \qquad \dot{\eta} = -\frac{\partial G}{\partial \chi}\dot{\gamma} \tag{5.6}$$

$$\dot{d}_i = l_i(t_i, Y_i, \chi; d_i)\,\dot{\gamma} \qquad i = 1,2,3 \tag{5.7}$$

$$F \leq 0 \qquad F\dot{\gamma} = 0 \qquad \dot{\gamma} \geq 0. \tag{5.8}$$

In the Equations above, $[u]^e$ is the elastic and $[u]^p$ is the plastic displacement jump. E is the free energy per unit surface in isothermal condition,

d_i are the damage variables, while K_i are interface stiffnesses. Operators $<>_-$ and $<>_+$ return the negative or positive parts of their argument, respectively. $\Psi(\eta)$ is the energy per unit surface corresponding to micromechanical rearrangements. In the Equation 5.5, F is the damage-yielding function and G is the plastic potential. $\dot{\gamma}$ represents the plastic-damage multiplier. Corigliano [52] investigated the general interface law in three specific cases, one of which, the elastic-damage model, will be discussed, according to the fact that it represents the glass frit behavior described in the previous Section.
In this case, $\Psi(\eta)$ and G are equal to zero. Hence the damage function, F, becomes:

$$\begin{aligned} F = F(Y_i, \bar{Y}) = f(a_1'' Y_1 + a_2'' Y_2 + a_3'' Y_3) - \bar{Y} - 1 \\ \dot{d_i} = l_i(\bar{Y})\dot{\gamma} \qquad i = 1,2,3 \qquad \dot{\bar{Y}} = \dot{\gamma} \end{aligned} \tag{5.9}$$

a_i are non-negative model parameters. The damage evolution law is:

$$\begin{aligned} d_i = L_i(\bar{Y}) \equiv \int_0^{\bar{Y}} l_i(\bar{Y}')d\bar{Y}' \qquad i = 1,2,3 \\ \bar{Y} = max\left\{1, \underset{\tau' \leq \tau}{max}\left\{f\left(\sum_{i=1}^{3} a_i'' Y_i(')\right)\right\}\right\} \end{aligned} \tag{5.10}$$

5.6.2 Two-dimensional fracture mechanics based on cohesive law

By exploiting a cohesive zone model and introducing it into the FEM, based on the formulation by Ortiz and Camacho [56], the interface law is applied on the common edges of the elements. In this way, the fracture between two domains as well as inside the domain can be investigated. In this model, quadratic triangular elements are used.
Figure 5.13 and 5.14 show the traction-displacement jump relationship in tensile and shear loading regimes. According to the Camacho-Ortiz model, the creation of new surfaces is based on the cohesive law described above (Figures 5.13 and 5.14) at the elements boundaries. It means that when the effective stress (see Equation 5.11) reaches the fracture stress (σ_0 or τ_0), crack initiates by means of duplicating the midnode.

$$\begin{aligned} \sigma^{eff} = \sqrt{\sigma^2 + \beta_t \tau^2}, \qquad \sigma \geq 0 \\ \sigma^{eff} = \sqrt{\beta_t}\langle|\tau| - \bar{\mu}|\sigma|\rangle, \qquad \sigma < 0 \end{aligned} \tag{5.11}$$

In this Equation, considering the mixed-mode fracture regime, β_t is a shear stress factor and $\bar{\mu}$ is the friction coefficient [57, 58]. After crack initiation,

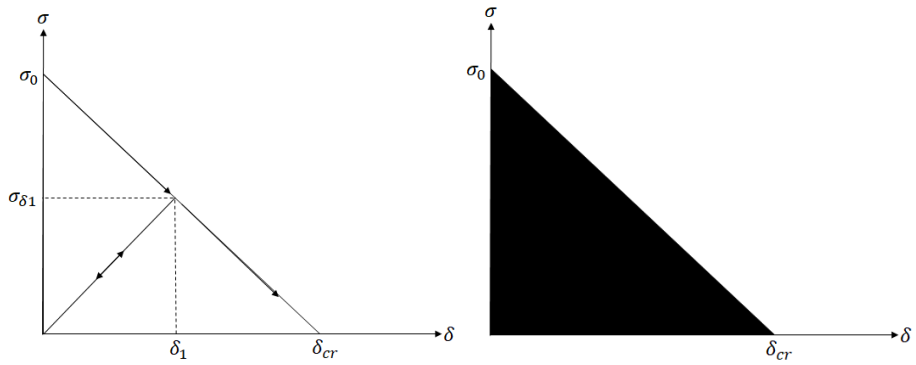

Figure 5.13: *Tension cohesive relation*

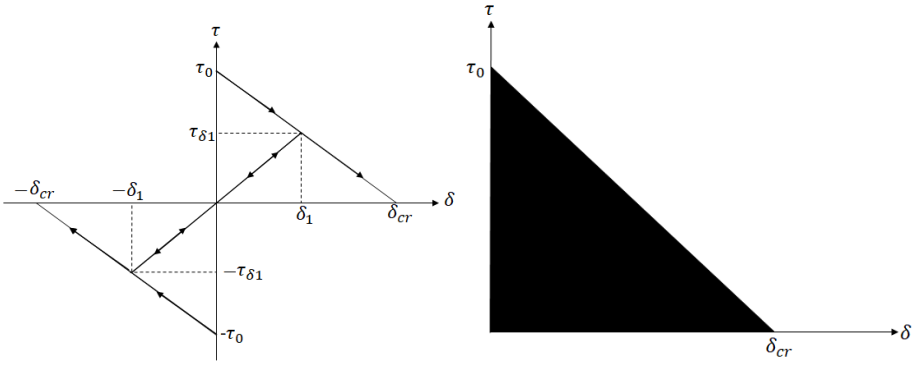

Figure 5.14: *Shear cohesive relation*

the propagation path can be either in the same direction or divert towards the other adjacent elements (Figure 5.15). Below, the algorithm of the frac-

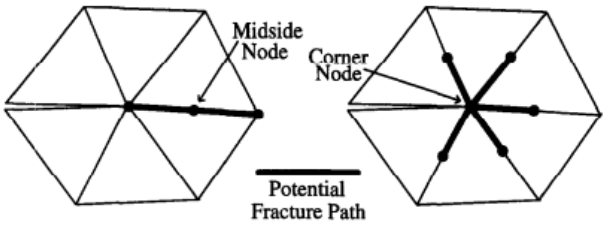

Figure 5.15: *Potential crack propagation path [56]*

ture, used also in the case of simulation of die shear test is demonstrated.

i) Choose a body in case a of multibody model and initialize it by index-

ing K_{body}=1.

ii) Gather midside nodes in the body K, and the elements attached to it, and identify the node with K_{mid} =1;

iii) Compute the effective stress at midside nodes, if it is higher than the fracture criterion, a crack is created by doubling the midside node.

iv) If $K_{mid} < N_{mid}$, where N_{mid} is the total number of midnodes in the body interior, goto iii.

v) Gather exterior corner node of body K, and the elements attached to them, identified by the index K_{cor}=1.

vi) Compute the effective stress at corner nodes, if it is higher than fracture criterion, crack is created by doubling the corner node.

vii) If $K_{cor} < N_{cor}$, where N_{cor} is the total number of corner nodes, goto vi.

viii) If $K_{body} < N_{body}$, where N_{body} is the total number of bodies in the model, goto ii.

The elements used in this simulation are 6-node (quadratic) triangles, with three Gauss points at the midpoints of the edges. The other important parameter in modelling the cohesive law is the characteristic length. There are different parameters that determine this length in different fracture modes: for the first mode, i) the cohesive strength, $\hat{\sigma}$, i.e. the maximum stress that an element can experience in the crack plane, ii) the mode I toughness, Γ_I, i.e. the energy dissipated by creating a unit area of new crack surface, iii) the effective modulus of the material on both side of the interface. The nominal mode-I fracture characteristic length is:

$$\begin{aligned} \zeta_I &= \frac{\bar{E}^* \Gamma_I}{\hat{\sigma}^2}, \\ \bar{E}^* &= \frac{\bar{E}_1 \bar{E}_2}{\bar{E}_1 + \bar{E}_2} \end{aligned} \tag{5.12}$$

where $\bar{E}$ is the plane stress modulus, and the 1 and 2 indices are related to the materials around the interface. If the ratio of the nominal fracture characteristic length to a geometrical dimensions related to fracture is less than 0.4, the crack growth is controlled by toughness [59]. If the instantaneous displacement from the equilibrium separation of the interface is δ_n, and the

cohesive traction has done a work W_I, the cohesive length is:

$$\xi_I = \frac{\bar{E}^2 \delta_n^2}{W_I} = \frac{\bar{E}^* W_I}{\sigma_{avg}^2} \tag{5.13}$$

where σ_{avg} is the average stress exerted by a cohesive element up to the displacement of interest. In order to simulate the cohesive zone by a FEM, there should be at least five Gauss points lying in a characteristic length. Hence, the element size is chosen $\xi_I/5$.

5.6.3 Numerical results

The 2-D model has three domains, the two silicon layers and the glass frit in between. The model is considered as plane strain; silicon mechanical properties are anisotropic with cubic symmetry and glass frit is isotropic. The other parameters considered in this analysis are the material strength at the common interface between the elements of the same or different domains, in order to set the criterion for the crack propagation path (see Figure 5.15). The last material inputs are the first and second mode energy release rate of each domain. Figure 5.16 shows the model imported to the MEMSYS

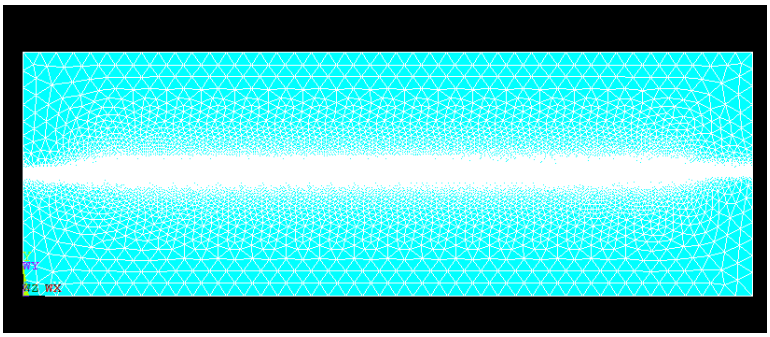

Figure 5.16: *Finite element model used for CZM modelling*

code, developed in the MEMS group at Politecnico di Milano, based on the algorithm presented in Section 5.6.2. Due to the high mesh density difference in the domains, the latter are subdivided in order to have the elements with sizes proper to the cohesive length and a smooth transition to prevent instability of the analysis. At the first region of the glass frit layer, the element size is 20 nm and it expands towards the domain with the factor of 1.2. The analysis is dynamic exploiting a mix of implicit-explicit time integration approach. As boundary conditions, all DOFs of the lower silicon layer are set to zero displacement, while similarly to the working principle of the

die shear test, a horizontal displacement is imposed on the lateral side of the above silicon layer. Table 5.2 shows the values for material properties used in the model. A compressive stiffness is introduced to prevent the element

Silicon	
Property	Value
Constitutive behavior	Anistropic
Maximum strength	1 GPa
Maximum boundary strength	1 GPa
Critical energy release rate	7 Pa·m
Compressive stiffness	10 GPa
Glass Frit	
Property	Value
Maximum strength	700 MPa
Maximum boundary strength	700 MPa
Critical energy release rate	10 Pa·m
Compressive stiffness	10 GPa

Table 5.2: *Material properties*

interpenetration.
The crack initiation and propagation path for the limited primary time steps are captured for the pure shear and the mixed mode fracture. Figures 5.17 and 5.18 show the crack initiation and propagation path for the shear mode and mixed-mode, respectively. The solid lines represent the edges of elements, where the stress reached its maximum value. The doubled lines (see Figure 5.18.c) represent the crack. At these edges, as mentioned, the nodes are duplicated to create the crack surfaces. In pure shear, first the crack is formed at the interface of the domains (glass frit), then the microcracks initiate in the silicon domains as well, due to the change of loading condition at the crack tip.
In the mixed-mode, due to the presence of the axial load, the crack is formed in the lower silicon layer as well. In this case, the crack propagation path is completely inside the lower part of the die.
Although the code provides the average load-displacement curve for the nodes at which the displacement is imposed, because of the very short time steps for explicit analysis (10^{-13}s) and because the analysis stops after some time steps, load-displacement data is not sufficient to compare with the experimental data.

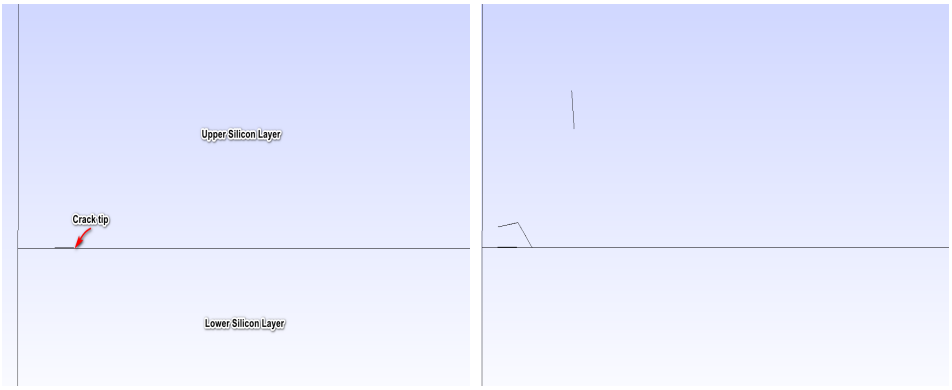

(a) *Crack in domain at* $1e^{-12}s$ **(b)** *Crack in domain at* $1.6e^{-12}s$

(c) *Crack in domain at* $2.4e^{-12}s$ **(d)** *Crack in domain at* $4.2e^{-12}s$

Figure 5.17: *Cracks and their propagation path in pure shear mode*

5.6.4 Die Shear Test Model with FEM

The die shear test also is modelled with finite elements, using interface element in a commercial finite element code, ANSYS. INTER203 (in ANSYS acronyms) element is used for the glass frit. This kind of element has zero thickness at the start of the analysis, which means the upper and lower nodes are geometrically coincident (see Figure 5.19a).

The constitutive behavior for this element is almost similar to the one discussed in Section 5.6.1, with the difference that in ANSYS the model is bilinear, i.e. the traction increases to the maximum value and then the degradation phase starts. The relation between traction and displacement jump is assumed linear, for both normal and tangential directions (Figure

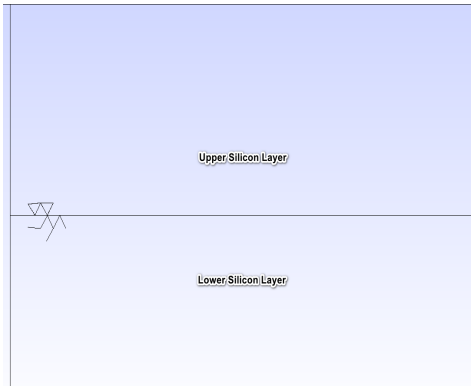

(a) *Crack in domain at* $1e^{-12}s$

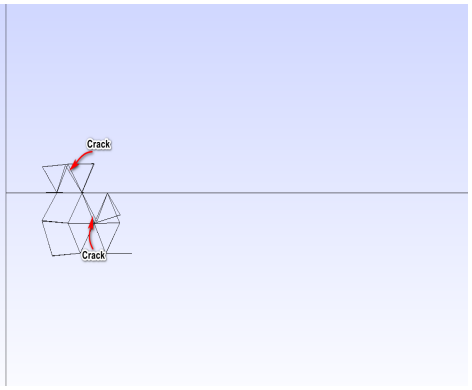

(b) *Crack in domain at* $1.6e^{-12}s$

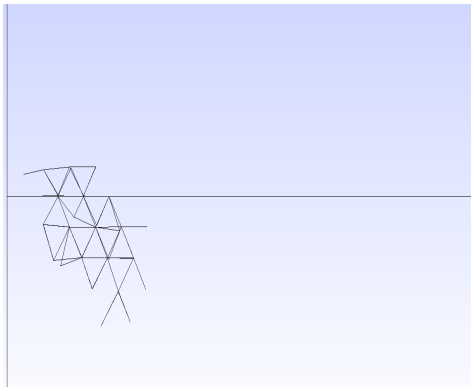

(c) *Crack in domain at* $2.4e^{-12}s$

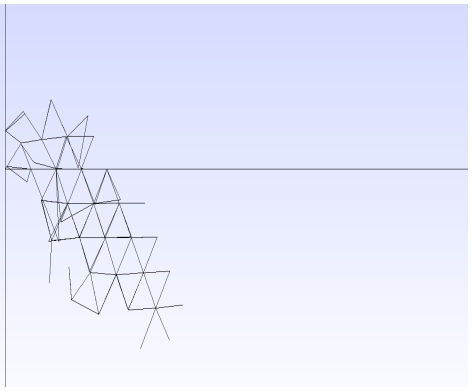

(d) *Crack in domain at* $4.2e^{-12}s$

Figure 5.18: *Cracks and their propagation path in mixed mode*

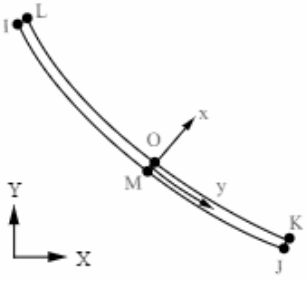

(a) *ANSYS INTER203 element*

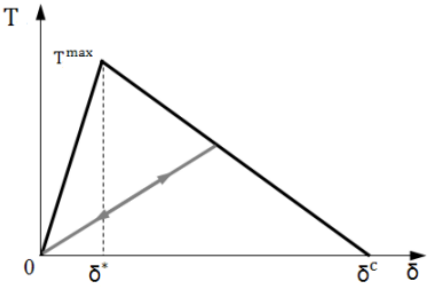

(b) *Cohesive zone model*

Figure 5.19: *Interface element and its constitutive behavior*

5.19b):

$$T = K\delta(1 - D) \tag{5.14}$$

In this model, by specifying the ratio between the displacement jump at the maximum traction and the final displacement value (at $T = 0$), the linear stiffness and the energy release rate of the material is defined. The maximum traction value in this model can be either positive or negative. A negative value for maximum traction in a specific mode means that the other fracture mode is dominant in the model. A positive value for all the modes represents the mixed-mode fracture.

For the sake of symmetry, just one half of the die is modelled. For the silicon layers, quadratic cubic elements are selected (SOLID186). The model is consisting of 155,200 and 169,930 elements and nodes, respectively. For the boundary conditions, similar to the previous analysis, the bottom and lateral faces of the lower silicon are fixed and the displacement is imposed on the face of the higher silicon layer. An implicit time integration analysis is carried out. Due to the limitation of this FE code regarding the simulation of crack growth in dynamics, only the pure shear and the mixed mode failure are modelled. In the pure shear mode failure, the displacement is imposed along the interface elements plane, while in the mixed mode, the imposed displacement is inclined with respect to the glass frit deposition plane. The displacement rate is set equal to the values used in the experimental phase.

Figure 5.21 shows the load-displacement curve obtained from ANSYS compared with the experimental die shear test. The results show an acceptable agreement between the model and the real data. As the constitutive behaviour defined in ANSYS is only linear, the non-linearity is not captured in the numerical analysis.

For the second failure mode, to replicate the load conditions during the test, the displacement is applied with inclination with respect to the interface elements initial plane. The fracture behavior of glass frit in tensile mode obtained from the study by Boettge et al. [45]. The results of the mixed mode fracture are presented in Figure 5.22. As shown in 5.22, the two-step behavior is also seen in the FE results. The right axis of the plot refers to the derivative of the load with respect to the variation of displacement. The slope is changed at the middle of the analysis. Two-step behavior shows that, first, the load reaches the maximum tangential stress; however, the normal stress does not reach the failure stress. Hence, glass frit resists until the load reaches its maximum value and the die finally fails. The out of plane displacement (displacement in the z-direction) of the upper silicon layer is different with respect to the first mechanism (pure shear failure),

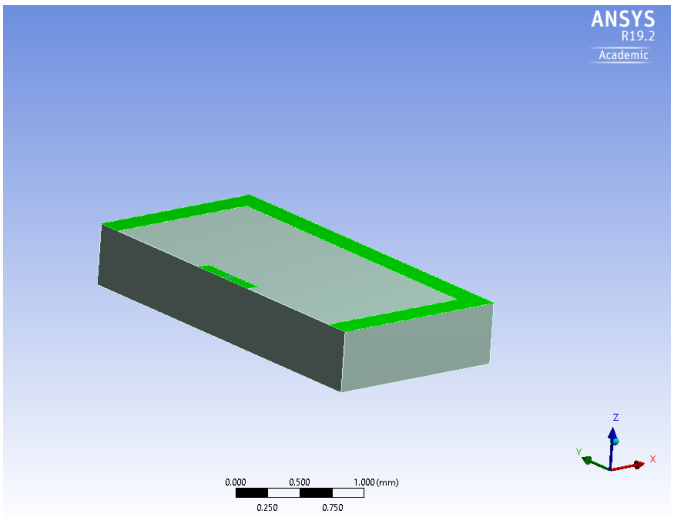

(a) *Area where interface elements placed for glass frit*

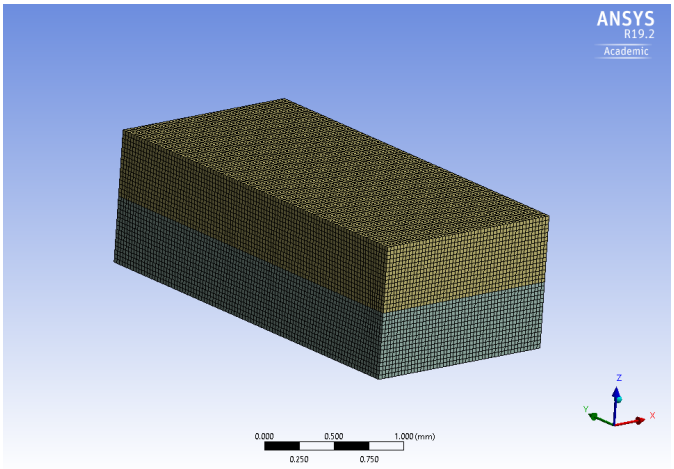

(b) *FE model for die shear test*

Figure 5.20: *Die shear test model in ANSYS*

where after the detachment of glass frit, the upper silicon remained on the die (the displacement in the z-direction is zero).
About third failure mechanism, i.e. silicon damage, the ANSYS is not able to model the crack growth in the transient analysis. Therefore, modelling this mechanism with this commercial finite element code is not possible.
As the interface elements replicate the behavior of the glass frit, these elements and the cohesive zone model are advantageous, in the sense of decreasing the total number of elements and, consequently, the computation

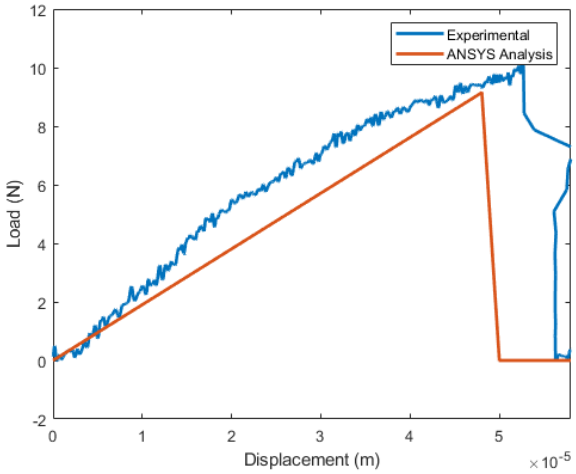

Figure 5.21: *Comparison between the results obtained by the FE model and the experiments for die shear test at a displacement rate of 10 μm/s*

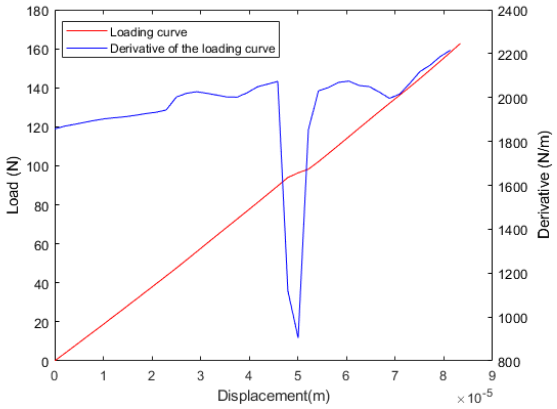

Figure 5.22: *Load-displacement curve for the mixed-mode failure*

time. In the next Chapter, the glass frit bonding process exploiting interface elements and CZM is discussed.

CHAPTER 6

3D Model and Simulation of Glass Frit Bonding

6.1 Introduction

The FEM is the main tool used for modelling and simulation of microsystems. Despite the method was introduced in 1940s for solving structural problems, nowadays it is widely used for simulation not only for single-field problems, such as structural, heat transfer, electrical, magnetic or fluid dynamics problems, but also coupled problems, combining the aforementioned physics.
Up to now, there is no a significant numerical study of the glass frit bonding. Ebert and Bahdahn [60], by using the FEM, have calculated the residual stress in the glass frit bonding with different width and thickness values, while the initial point of their studies is the cooling phase. They observed a significant residual stress within the bonding frame. Therefore, by exploiting the experimental results presented in this dissertation, in this Chapter glass frit bonding modelled via FEM is presented. Sandvand et al. [61] also investigated the effect of bonding material distribution on the residual stress of glass frit bonded pressure sensor, utilizing the FEM.

All the simulations have been performed by a commercial code, ANSYS® Academic Research Mechanical, Release 18 and 19.

6.2 The Models

The model both in 2- and 3-dimensions consists of two bond tools, which are holding the silicon wafers in the bonding chamber, two silicon wafers and, in between them, the binder, i.e. glass frit (see Figures 6.1 and 6.2). The dimensions of each body are presented in Table 6.1. Moreover, the material properties are reported in the Tables 6.2 and 6.3. Bond tools are made of stainless steel and titanium; these materials together with glass frit are considered as isotropic and elastic, while silicon is a monocrystal, with cubic symmetry, whose stiffness matrix has the following aspect:

$$C = \begin{bmatrix} C11 & C12 & C12 & 0 & 0 & 0 \\ C12 & C11 & C12 & 0 & 0 & 0 \\ C12 & C12 & C11 & 0 & 0 & 0 \\ 0 & 0 & 0 & C44 & 0 & 0 \\ 0 & 0 & 0 & 0 & C44 & 0 \\ 0 & 0 & 0 & 0 & 0 & C44 \end{bmatrix} \tag{6.1}$$

Equation 6.1 presents the simplified fourth order elasticity tensor, where C11, C12 and C44 are the constants of the stiffness matrix. It is worth to mention that silicon mechanical properties are temperature dependent. In Figure 6.3, the relationship of silicon elastic modulus and temperature is reported, based on the formula presented in [62]. Due to cubic symmetry, the elastic properties of monocrytalline silicon also can be presented in terms of an orthotropic material. Based on the orientation of the wafer, the orthotropic constants are equal to values reported in Table 6.2 [63].

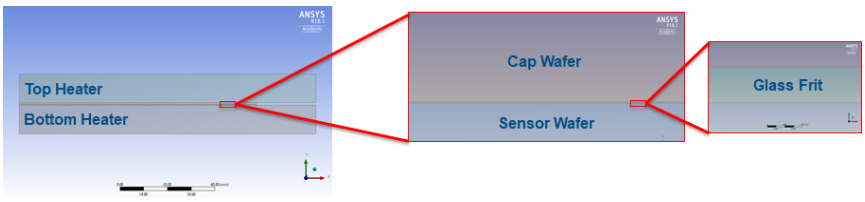

Figure 6.1: *Axisymmetric model of glass frit bonding*

The connection between the parts (i.e. the two wafers, the bond tools and the glass frit layer) are defined by contacts. More precisely, the interfaces

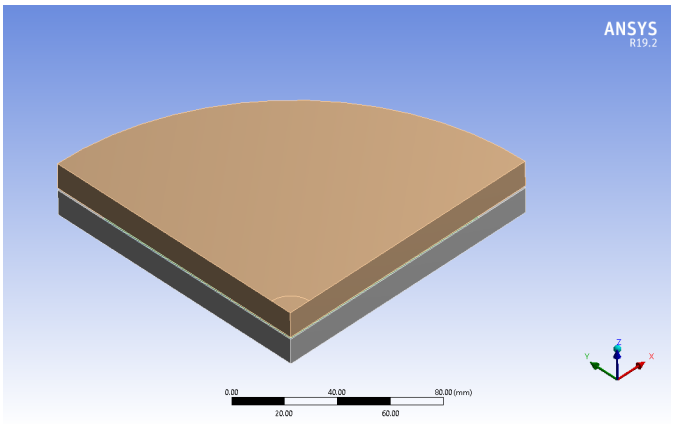

Figure 6.2: *Three dimensional model for glass frit bonding*

Part	Radius (mm)	Height (mm)
Bond tools	250	12
Silicon wafers	200	0.725
Glass frit layer	200	0.02

Table 6.1: *Geometrical dimensions of the model*

Material	Elastic moduli (GPa)	Poisson's ratio
Titanium	96	0.36
Stainless steel	193	0.31
Silicon	$E_x = E_y = 169, E_z = 130$	$\nu_{xy} = .064$
	$G_{xy} = 50.9, G_{xz} = 79.6$	$\nu_{yz} = 0.36$
	$G_{yz} = 79.6$	$\nu_{xz} = 0.28$

Table 6.2: *Mechanical materials properties*

Material	Thermal conductivity ($Wm^{-1}°C^{-1}$)	Thermal expansion coefficient ($°C^{-1}$)
Titanium	21.9	9.4×10^{-6}
Stainless steel	15.1	1.7×10^{-6}
Silicon	124	2.46×10^{-6}

Table 6.3: *Thermal materials properties at room temperature*

between the bond tools and silicon are modelled by a unilateral contact with no friction. The glass frit and the silicon wafer are attached ("bonded" according to ANSYS acronyms), which means that their DOFs are coupled to each other. The remaining contact area, i.e. between the glass frit and the sensor wafer, has a changing property. As discussed in the Section 2.3.4, the glass frit wets completely the adjacent surface at the temperature above

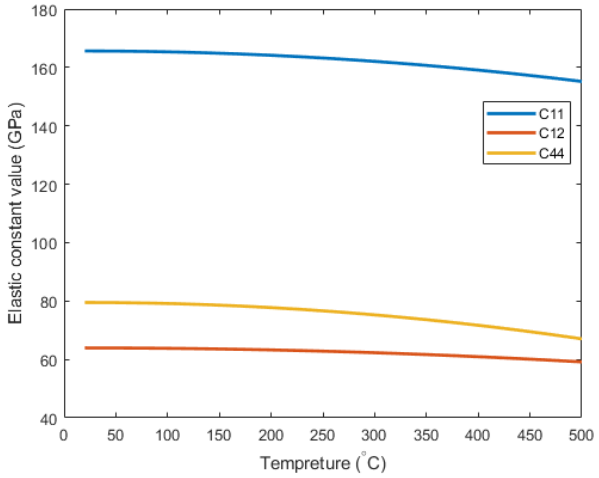

Figure 6.3: *Elastic constants variation vs temperature for silicon*

430 °C. Hence the chemical bonds start to develop at this point. To model this behavior, in the 2-D model the connection is set to unilateral frictionless contact until the temperature reaches 430 °C. Then, the contact property is changed to "bonded", assuming that the secure between the parts has been achieved. In 3-D, as the glass frit layer is modelled by interface elements, at the same temperature level the shear stiffness is changed to the real value obtained in the Chapter 5.
The boundary conditions applied to the model are:

- at the bottom surface of the lower bond tool all the DOFs are restrained (zero displacement);
- there are two grips holding mechanically together the silicon wafers during the bonding process (see Figure 6.4), modelled as a region where the nodes DOFs are set to zero.
- an upper pressure is applied on the above bond tool;
- temperature sources are set for both bond tools as hot bodies as well as at the surface along the perimeter of the silicon-glass frit-silicon structure, which is exposed to equal temperature by convection.

In the bonding chamber, mechanical pressure and temperature variation are applied simultaneously to the Si-gf-Si system. Figure 6.5 shows the thermal and mechanical load cycle in the bonding chamber. Because of confidentiality issues, the values and the changing rates can not be reported in this

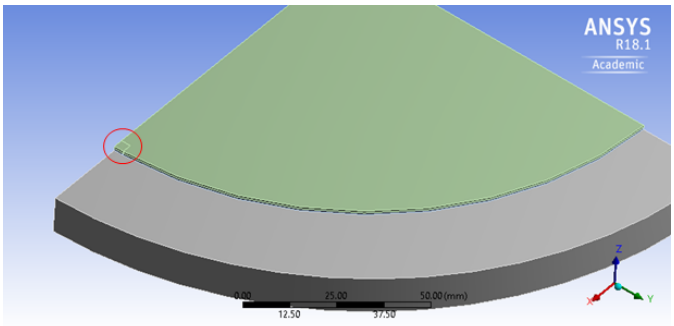

Figure 6.4: *Bond tool grip zone on the wafers*

dissertation. There are some points indicating to the different stages of the bonding on the plot, which will be used in the results Section as the referring points to a specific part of the process. In the following Sections, first

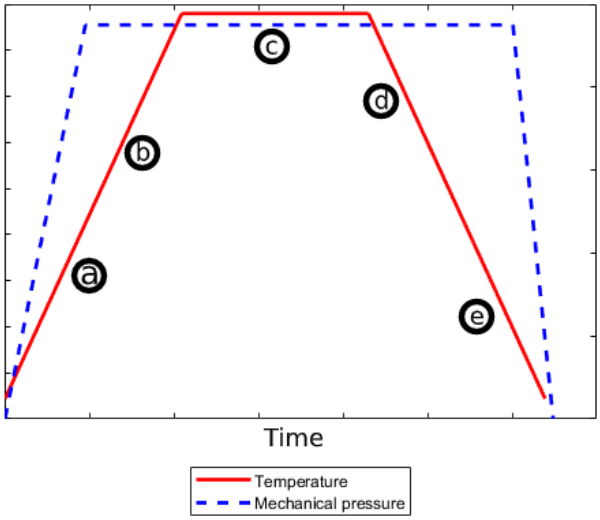

Figure 6.5: *Thermomechanical loading sequence in the glass frit bonding*

the thermal analysis and then, the temperature distribution in the bodies are presented. Finally, the warpage and the residual stresses resulting from the complete thermomechanical glass frit bonding will be discussed.

6.3 Thermal Analysis

The temperature distribution in a body is described by the heat flow equation:

$$\frac{\partial}{\partial x}(K_x\frac{\partial T}{\partial x}) + \frac{\partial}{\partial y}(K_y\frac{\partial T}{\partial y}) + \frac{\partial}{\partial z}(K_z\frac{\partial T}{\partial z}) + q_v = \rho c_p\frac{\partial T}{\partial t} \tag{6.2}$$

where $T = T(x,t)$ is the body temperature, q_v is the rate at which the energy is generated per unit volume, K_i is the thermal conductivity, ρ is the material density and c_p is specific heat capacity.
By performing a transient thermal analysis, the temperature distribution in the Si-gf-Si system, when it is in the bonding chamber, based on the thermal sources and boundary conditions described in the previous Section, is presented in Figures 6.6 and 6.7, for the 2- and 3-dimensional models, respectively. As it can be observed, the temperature distribution is homogeneous along the bodies, as the Si-gf-Si system thickness is less than 2 millimeters and in direct contact with the heat sources.
By measuring the temperature at several points of the thermocouple wafers, it can be seen that the maximum temperature difference with respect to the source temperature is 6 °C. Therefore, it can be concluded that the variation of thermal stress is out of scope as for what it may concern the sources causing the residual stress in the bonding process.

6.4 2D Axisymmetric Results

In the axisymmetric model, quadratic plane elements have been used (PLANE 183 in ANSYS® acronyms). Also, the glass frit is considered a homogeneous layer along the silicon wafer. Material properties assigned to glass frit, as attained from the nanoindentation test (see Section 4.3), are presented in Table 6.4. The number of elements and nodes for this model is

Property	Value
Elastic modulus	85 GPa
Poisson's ratio	0.17
CTE	$7\times10^{-6}\ °C^{-1}$

Table 6.4: *Properties assigned to glass frit for the axisymmetric analysis*

165,339 and 512,559, respectively.
At the end of a full thermomechanical cycle, the numerical out of plane deflection is obtained; it is in the range reported in actual production after

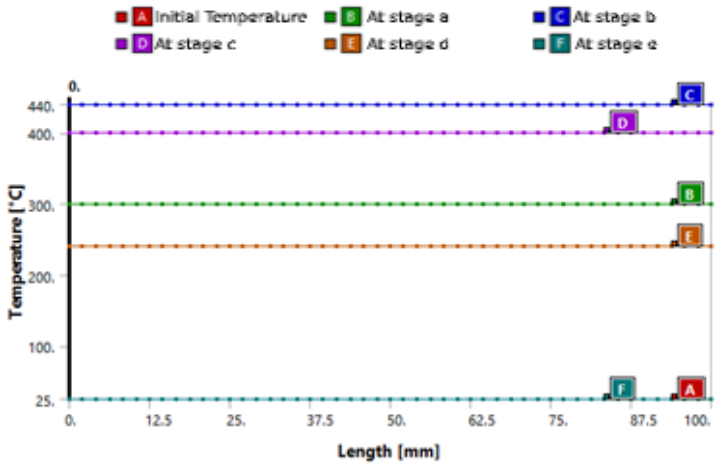

(a) *Temperature along the length at various times*

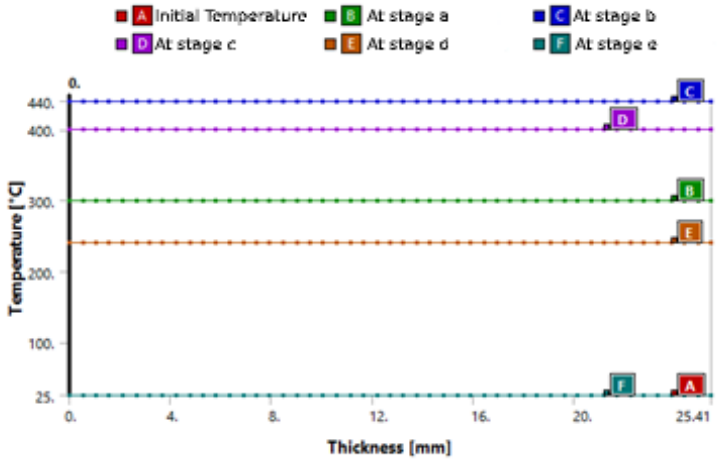

(b) *Temperature along the thickness at various times*

Figure 6.6: *Temperature distribution in 2-D model*

glass frit bonding in the clean room. The final shape of bonded wafers, as discussed in Chapter 3, is spherical, i.e. the local curvature is constant along the wafer (see Figure 6.8) with the maximum out of plane deflection equal to 104 μm. There are two assumptions in the axisymmetric simulations that do not represent the actual bonding. First, the glass frit is not a homogeneous layer, but it is deposited in a rectangular glue line on the cap silicon wafer. Second, the circumferential edge of the wafers and glass

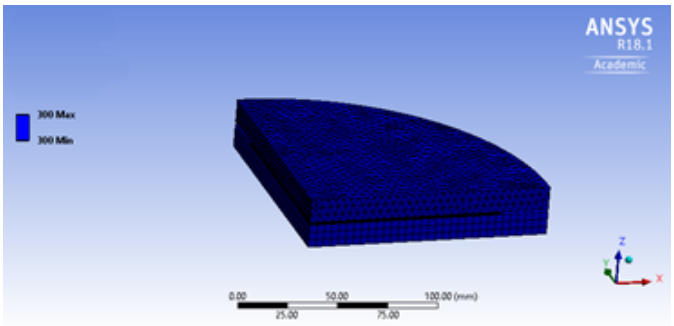

(a) *Temperature in bodies at stage b*

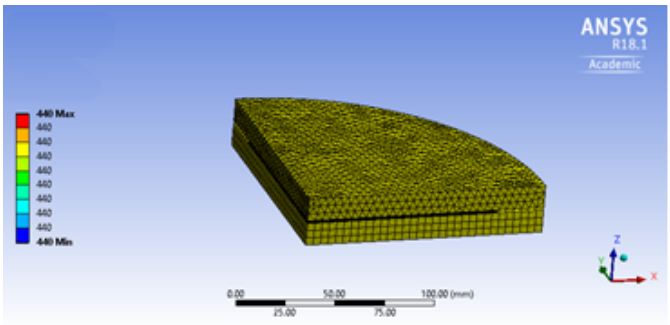

(b) *Temperature in bodies at stage c*

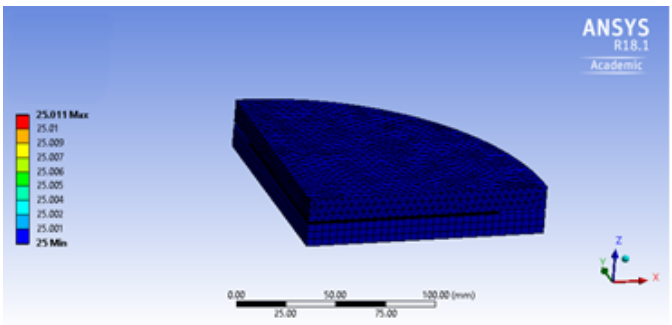

(c) *Temperature in bodies at stage f*

Figure 6.7: *Temperature distribution in 3-D model*

frit is clamped, in order to impose the grip effect. Based on the nature of 2-D axisymmetry, all the wafer edges are clamped, while the grip is just applied on two points along the edge. Hence, due to this overconstraint, the deflection is assumed to be higher than the real value.

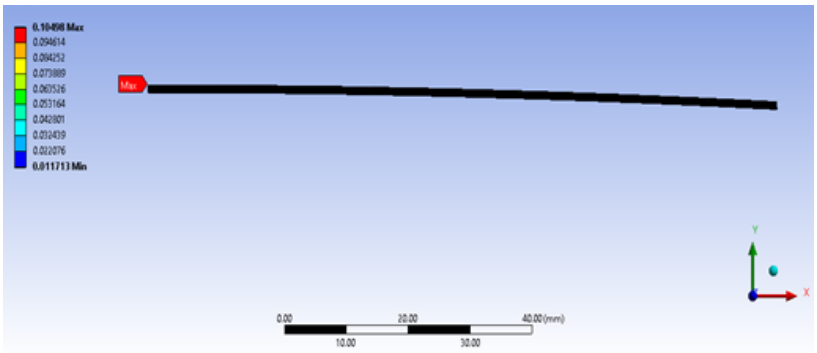

Figure 6.8: *Out of plane deflection in the axisymmetric analysis in millimeters*

6.5 3D Model Results

In the three-dimensional model, for the sake of symmetry, 1/4 of the bonding chamber has been modelled. 20-node cubic elements (SOLID186 in ANSYS® acronyms) have been chosen for each part of the model. As for the glass frit material interconnecting the two silicon wafers, because of its small thickness with respect to the silicon wafers and the rest of the model, an unfeasible number of solid elements would be generated: therefore, 8-node interface finite elements (INTER205 in ANSYS® acronyms) are exploited to model the glass frit layer. The regions where these elements are implemented are the glue lines squares, where the glass frit is deposited surrounding the die (see Figure 6.9). In this type of elements, the consti-

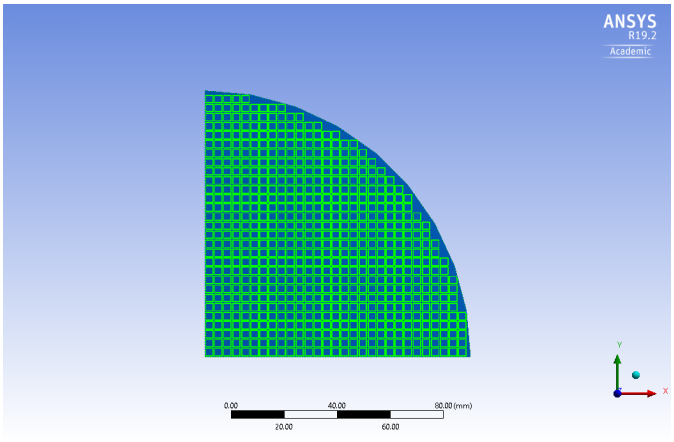

Figure 6.9: *Regions where the INTER205 elements are placed as glass frit*

tutive material behavior is defined through a cohesive zone approach (see Section 5.6.1) and their topology does not require other nodes with respect to the ones at the two facing surfaces. A bilinear, traction-displacement discontinuity law, linearly increasing up to the maximum strength and then linearly decreasing from it down to zero, defines the behavior of the element (see again Chapter 5); it is adopted to describe the (shear debonding) mode II, because the large difference in the thermal expansion coefficient of silicon and glass frit is here supposed to trigger the warpage. The tangential

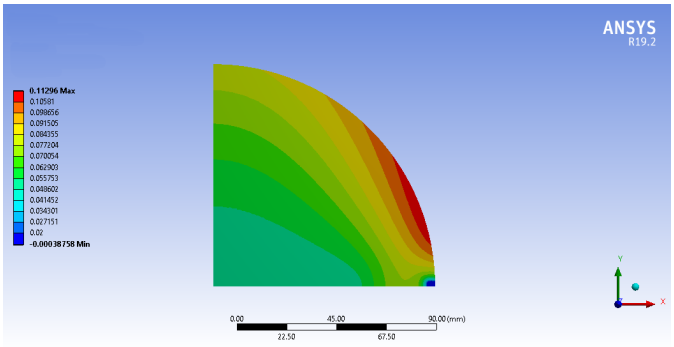

Figure 6.10: *Out of plane deflection for 3D model in millimeters.*

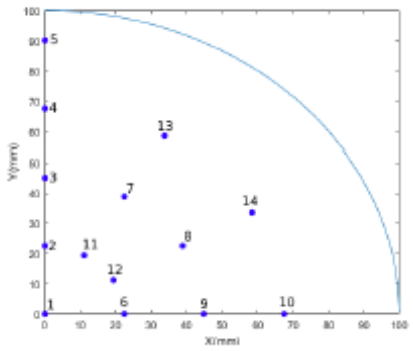

(a) *Coordinates of the point at which the results have been compared*

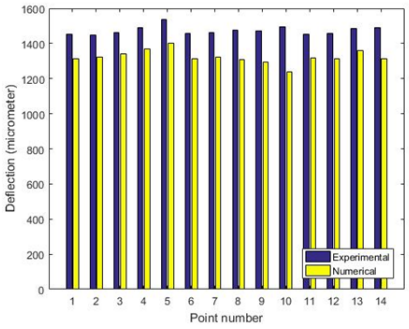

(b) *Z-height of the points in numerical and experimental measurement*

Figure 6.11: *Experimental and numerical results comparison*

stiffnesses in the interface elements are assigned according to the results obtained from the die shear test and from the numerical analysis for mode I fracture in glass frit. Here, the grip is modelled with the actual dimensions, so the overconstraint condition is deleted in the model. The result presented in Figure 6.10 shows the out of plane deflection of the silicon wafer in the

model, after the bonding process is completed.
In order to verify the model, the deflection in 14 different points on the wafer has been compared with experimental measurements. The experimental data are the average out-of-plane coordination of 21 sets of measurements. Figure 6.11 shows the results, and a good agreement between the numerical and experimental results is observed.
The difference between the values from models and experiments may come from following reasons:

- the anisotropic thermal expansion of silicon has been neglected;
- the glass frit behavior is considered constant during temperature variation;
- the constitutive behavior of glass frit has been simplified by assuming a linear relationship between the load and displacement.

CHAPTER 7

Wafers with Reduced Thickness

7.1 Introduction

According to the three-dimensional simulation results for glass frit bonding, there are two main sources that induce the residual stress in the system: i) the difference in the thermal expansion coefficient between silicon and the glass frit, ii) the inevitable mechanical constraints existing in the system, such as bond tools grips.
The initial solution for the first problem is to decrease the bonding temperature, which leads to a smaller thermal strain difference between silicon and glass frit. However, as it is presented in Figure 7.1, the bonding yield decreases with temperature. This causes a lower mechanical resistance as well as insufficient hermeticity properties. For the second issue, in order to diminish the effect of mechanical constraints, the idea is to provide a space for silicon to release the stress in the direction of the mechanical grip. Hence, at the center of both silicon wafers, in a circular area with a certain diameter, a thickness reduction at both faces is applied (see Figure 7.2). The reason why thickness reduction is chosen instead of a through hole resides in the depressurization applied at the interface of the bond tool and the wafer to hold the wafer on bond tool. The hole would break this de-

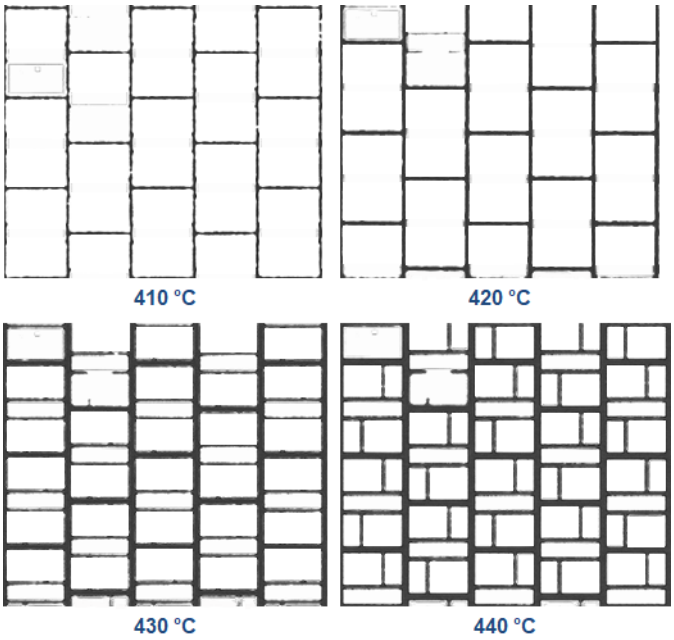

Figure 7.1: *Dependency of bonding yield on the bonding temperature*

pressurization and would disrupt the alignment and transportation process.

7.2 Model and simulation

First, the depth of this thickness reduction has been chosen equal to 150 μm, in order to maintain the mechanical stability of this part of the wafer. Then, to determine the optimal value for the radius, a parametric axisymmetric analysis has been carried out. Therefore, the maximum out of plane deflection versus the reduced-thickness zone radius decreases as shown in Figure 7.3. According to the results obtained, the optimal radius for the modified zone (reduced-thickness) turns out to be 3 mm. Hence, the geometrical modification has been applied to the 3-D model presented in Section 6.5. In the results, as shown in Figure 7.4, the deflection decreased to 58 μm from 87 μm, which indicates a 34% warpage decrease.

7.3 Experimental results

In order to verify the reduced thickness idea, wafers with the geometrical configuration discussed in the previous Section have been manufactured and bonded with glass frit. The silicon wafer subjected to the process is 8-

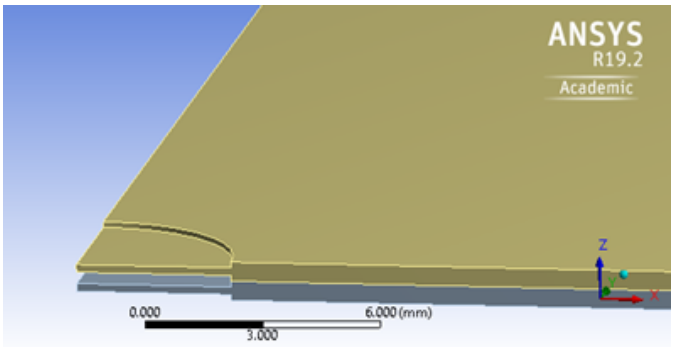

Figure 7.2: *Reduced thickness model*

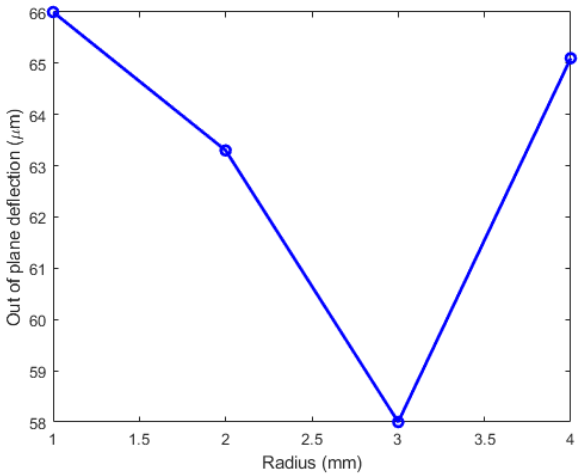

Figure 7.3: *Parametric analysis aimed to obtain the optimal radius*

inch type (8 inches in diameter and 525 μm thickness). The steps required to produce the wafers are as follows:

- growing silicon oxide on both sides of the wafer;
- deposition of resist upon the oxide;
- exposing wafer to the electromagnetic beam through the mask;
- dry etching process;
- glass frit deposition on the glue lines;
- thermomechanical glass frit bonding.

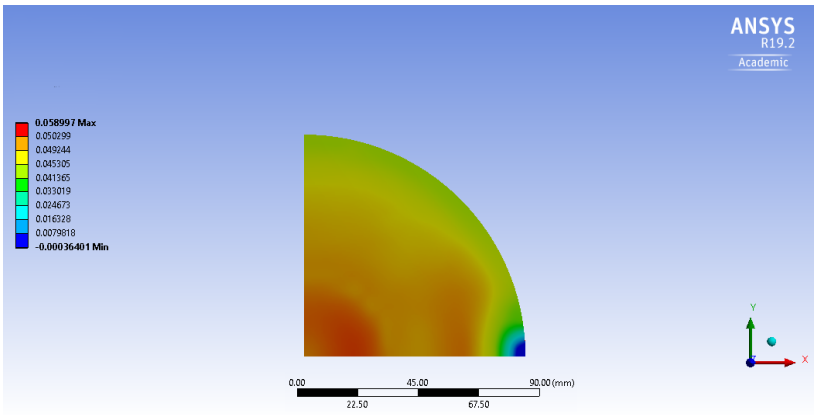

Figure 7.4: *Out of plane deflection contour plot for the geometrical modified wafers (in mm)*

Figure 7.5 shows the sketch of the mask used in order to specify the central region for the excessive etching as well as the glue lines for glass frit printing. The central region is etched at both wafer sides and, according to the configuration used in numerical analysis, etched for 150 μm. In order to discuss about the effect of the micromachining process on the residual stress, silicon wafers with plain surface are bonded as well, considered as reference specimens.

The results of out of plane displacement measurements, after the bonding process, for both sets of silicon wafers are next presented. Figure 7.6 shows the locations of the overall 49 points where measurements are taken on the silicon wafer. For each set of specimen groups, three pair of wafers are bonded with glass frit. Therefore, average data of these pairs are used in this Section.

In order to obtain the final shape of the wafers based on the measurements, by exploiting interpolation, the wafers surfaces are created. The mesh grid chosen for the interpolation is in the range of a -90:90 mm square surface, as the experimental data lie in this plane. The interpolation function is a cubic polynomial, in order to consider the change of slope as well as the curvature. The central point measurement (point no.29 in Figure 7.6) is not considered, due to the fact that this point is located in the reduced thickness region; hence, the data of this point can not be useful for the surface creation. The reference plane for measuring the deflection is assigned on the face of the upper silicon wafer; hence, the out of plane deflection for all the points are equal to zero before the bonding process. The interpolation process is performed with MATLAB R2019a with academic license.

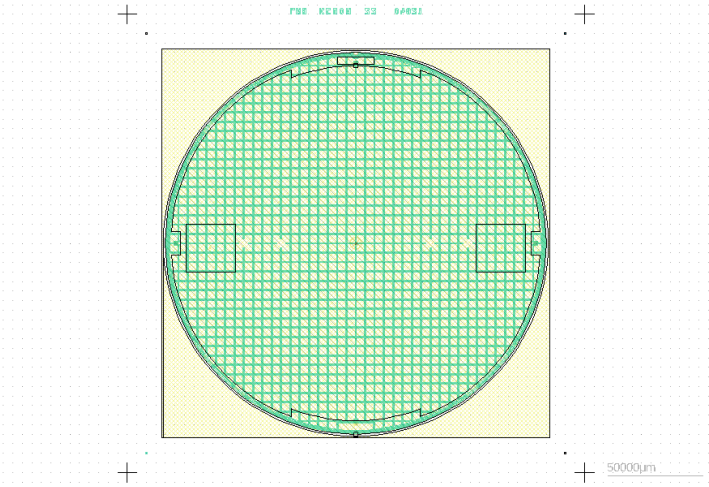

(a) *The sketch of the mask used for micromachining process*

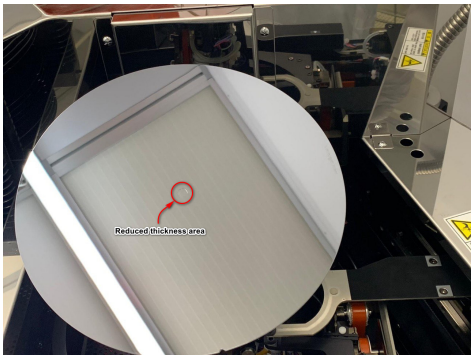

(b) *Silicon wafer with reduced thickness region*

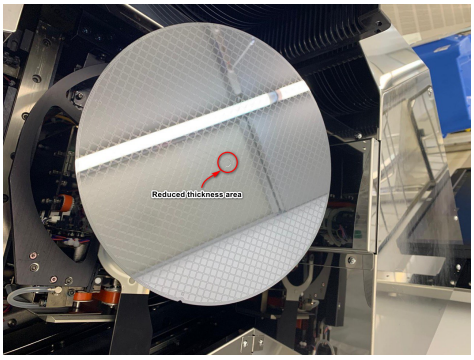

(c) *Silicon wafer with reduced thickness region on the side of glass frit*

Figure 7.5: *The mask and the silicon wafers produced by the new micromachining procedure*

Figures 7.7 and 7.8 are demonstration of the surface profiles for reference and reduced thickness wafers, respectively. A negative deflection value indicates that a concave shape for the wafers.

In order to study thoroughly the effect of the central etched region on the warpage of the glass frit bonded wafers, the contour plot for both sets of specimens are compared in Figure 7.9. The qualitative comparison between the deflection values shows that the overall warpage of the wafers fabricated with the proposed micromachining process is lower than the plain silicon wafers; specifically, in the central region. The difference in the out of plane displacement of both sets of specimens at the points 15-20,26-28 and 30-

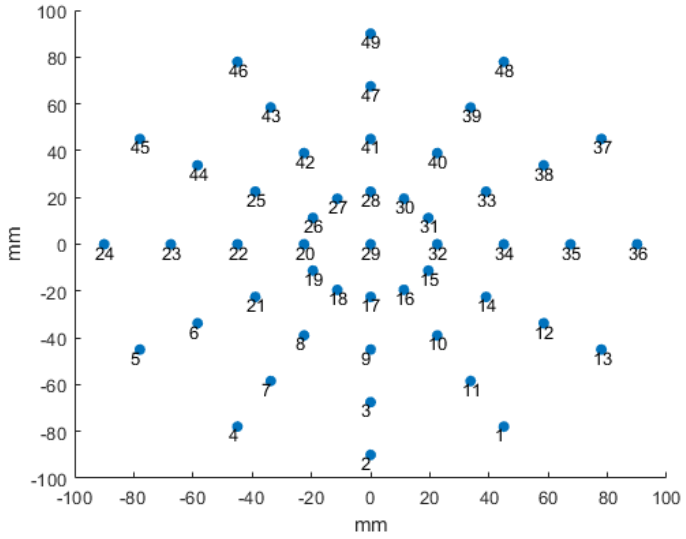

Figure 7.6: *49 measurement points coordination on silicon wafer*

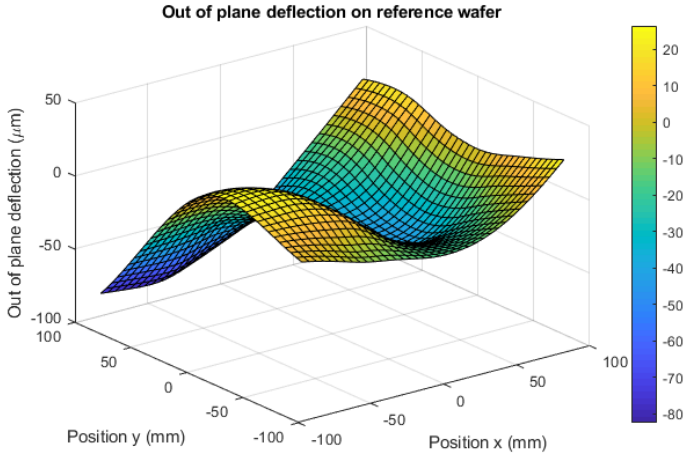

Figure 7.7: *Final shape of the reference bonded wafer*

32 which are close to the reduced thickness region (see Figure 7.6 for the coordinates) is reported in Figure 7.10.

As shown in Figure 7.10, the deflection is decreased at these points in the range of 17 to nearly 31 micrometers. Also in the simulations also at the central region, the out of plane deflection obtained is 29 micrometer lower than the plain wafer model (see Chapter 7). Hence, the experimental data

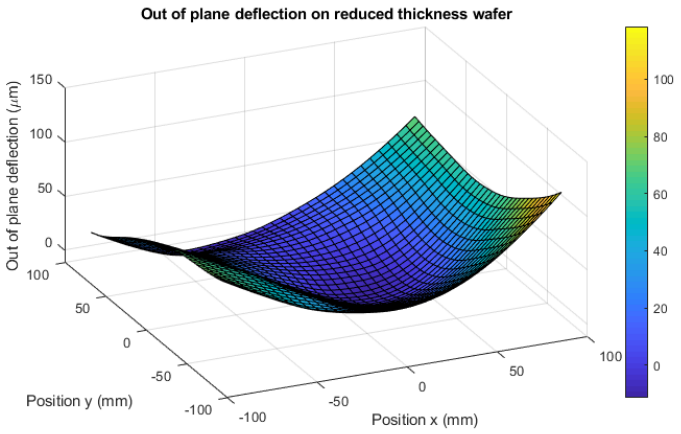

Figure 7.8: *Final shape of the bonded wafers with reduced thickness region*

are in accordance with the model and with the results of the simulation.
Another advantageous enhancement of the proposed micromachining process concerns on the overall shape of the bonded wafer. Figure 7.11 shows the superposed plot of the final bonded wafers, where the distorted part in the reference wafer is removed and substituted by a monotonic and uniform shape in the modified geometry samples.
As presented in Figure 7.5, even if the reduction region affects only 4 dies, however the warpage reduction is significant also for the dies surrounding this region. As the maximum warpage always occurs at the central part (as it can be seen from the reference wafers deflections in Figures 7.7 and 7.9.a), this process is a good compromise to reduce the possible damage to the other dies in the inner parts of the wafer, as well as the improving peculiar deformation of the dies placed at the edge of the wafer. Obviously, the bigger the diameter of the etched region, the less the residual stress for the surroundings area; however, this is a debate of how many devices should be sacrificed in order to protect other devices from the excessive residual stresses.
Another parameter for this micromachining process that has to be discussed is the value of etching depth. As the common silicon wafers used in the semiconductors industry are 4-inch and 8-inch wafers (with the thickness of 525 and 725 μm, respectively), it is important that the maximum value of etch depth prevents any fracture in the etched area. Also, as Barnat et al. discussed, the strength of silicon with different thickness varies [64]. As the thickness of the silicon decreased, its strength increases, although this strength variation depends on the surface topology as well. Barnet reported

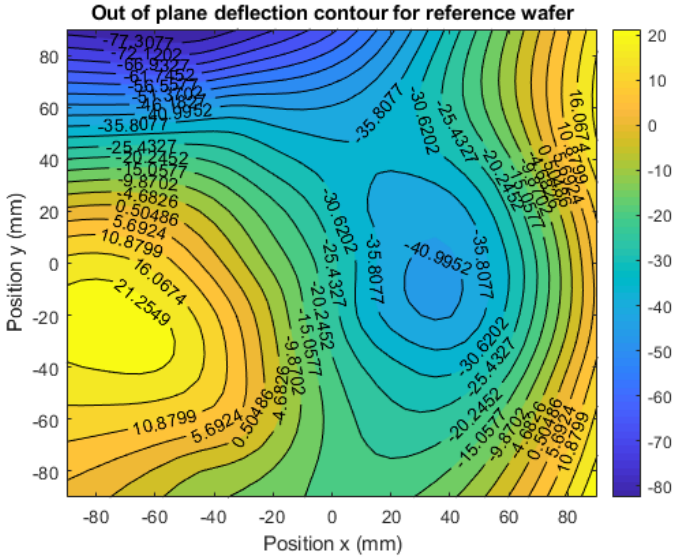

(a) *Reference wafer*

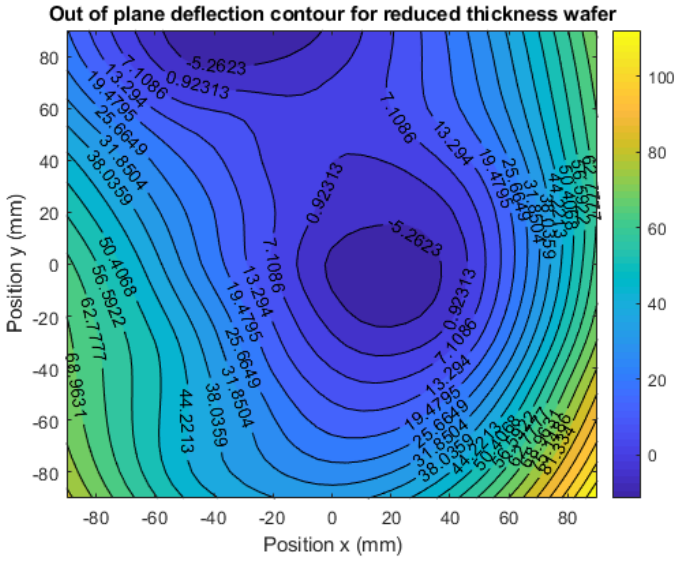

(b) *Reduced thickness wafer*

Figure 7.9: *Contour plot of the out of plane deflection for reference and etched wafers*

that the deflection of silicon under three point bending test depending on the surface treatment is between 100 to 300 micrometers. In the presented process, as the surface is reduced by etching, surface topology is much

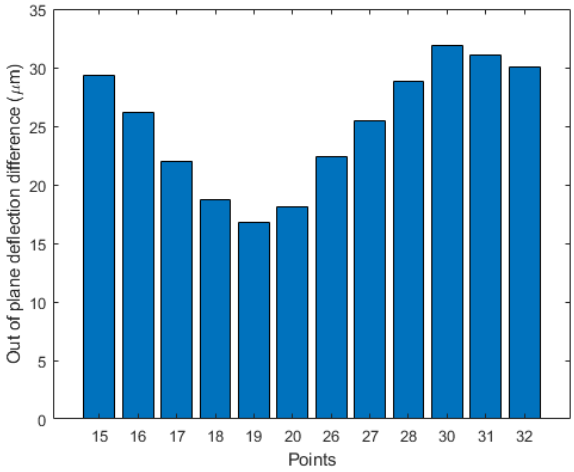

Figure 7.10: *Out of plane deflection reduction at points around the etched region with respect to the reference wafer*

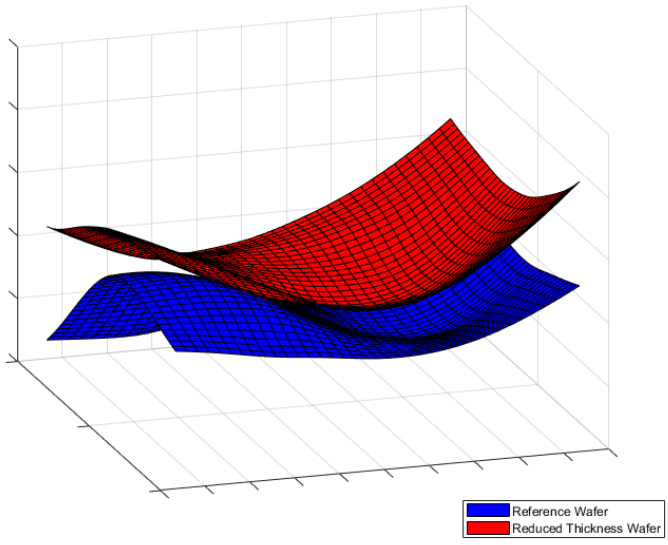

Figure 7.11: *Final shape comparison between plain silicon wafer and modified silicon wafers, after bonding with glass frit*

smoother with respect to the grinding. Therefore, the deflection in the proposed process is expected to be higher with respect to the wafers having reduced thickness by grinding instead of etching; hence in the proposed

process it is reasonable to expect that it is possible to reduce the thickness even more.

CHAPTER 8

Conclusion and Future Work

In this dissertation, one of the main and essential steps of the microsystems production is studied. Regardless of the device type, this process is applied to every silicon wafer as the first level packaging. Glass frit bonding, one of the categories in thermo-mechanical wafer bonding process, is the main focus and the decrease of the residual stress after this kind of bonding represents the main goal of this study. The main achievements and results of this dissertation are reported in the following paragraphs. Next, possible improvements and suggestions regarding wafer-level bonding are presented.
First, the Stoney formula is studied for the glass frit deposition as a thin film on silicon wafer. Also, the effect of film thickness on the residual stress in the wafer due to the thermal strain is discussed.
Since there is lack of data for glass frit properties, a series of tests to characterize this material are carried out. From surface topography, an arithmetic average height is obtained equal to 1.585 μm. Moreover, the thickness of deposited glass frit for bonding process is obtained, equal to 20.136 μm. The mechanical strength of the glass frit is measured by a nanindentation test. In order to control the uniformity of the properties, the tests are performed at the center and the edge of the wafer. The results show that the elastic modulus for the material is 85 GPa and its hardness is 5.3 GPa. The

results are similar for both sets of specimens. Also, the microstructural features of the glass frit are characterized by scanning electron microscopy. A disperse phase within the glass frit matrix with the areal percentage of 17.32% is observed. Moreover, the presence of the silicon in the glass frit layer due to the dicing process after bonding is observed. The chemical composition of each phase is also studied by Energy Disperse Spectroscopy. The disperse phase is found enriched by aluminum and magnesium oxide.

In the next step, the mechanical reliability of the dies bonded by glass grit is studied. The method used for this subject is the die shear test based on the military standard MIL-STD883E. In order to perform the test, first a specific stage is designed and fabricated to hold steadily the specimen. Results of the test, as the load-displacements curves, are studied and three types of failure mechanism are observed. The first mechanism is a pure shear failure, in which the die is unbonded only by the tangential mode. The lowest failure load is obtained for this mechanism (0.3 kgf). The second failure mechanism is the mixed-mode fracture. In this mechanism the load-displacement curve shows a change of slope. The reason relates to either the inclination of the specimen in the middle of the test (due to the exceeding of friction force between the stage and specimen) in higher displacement rates or the change of fracture mode due to the presence of silicon debris in the glass frit layer in lower rates. The last mechanism is the failure of die in the silicon medium. As observed by the digital microscope, the crack initiates and propagated through the silicon medium. In this mechanism the die is completely destroyed and it has the maximum failure load amongst all mechanisms. The cause of this failure is the stress concentration at the contact point between the silicon and the stage for the higher imposed displacement rates. In order to investigate numerically the crack initiation and propagation via cohesive zone model, the die shear test is modelled by FEs with cohesive zone models. The crack propagation path and the load-displacement curves are obtained and compared with the experimental data.

The glass frit bonding process is modelled by commercial FE code ANSYS first in an axisymmetric two-dimensional analysis. The transient thermal analysis shows a uniform temperature distribution within the silicon and the glass frit layers, due to the small thickness of the layers. Hence there are no thermal stresses within each domain. In order to replicate exactly the loading conditions and the glass frit area on the wafer, a three dimensional thermomechanical analysis is carried out, utilizing interface elements for glass frit, in order to reduce the computational cost. The deflection results

show a good agreement with the experimental measurements. The sources of the residual stress based on the simulation results are identified as the mismatch of the thermal expansion coefficients and the mechanical constraints, which are supporting the wafers in the alignments and the transportation to the bonding chamber.
In the last Chapter, as the sources of the residual stress are recognized, a solution is introduced by means of a micromachining process. A reduction of thickness at the central part of the silicon wafers on both wafers sides helps relaxing the expansion and reduce the effect of the mechanical constraints. The FE model of the new geometrical configuration shows a 34% warpage reduction. To verify this numerical result, wafers are produced and bonded with this feature and show that the out of plane deflection at the proximity of reduced thickness region is decreased up to 30 μm.

To further improve this study, there are some needs for the simulation of the process. As the cohesive zone model's constitutive behaviour in ANSYS is defined only either bilinear or exponential curves, the exact response of the glass frit under the load has to be introduced in the model to enhance it.
An advancement in the analytical solution for wafer-to-wafer bonding is another possible improvement for this work, based on studies on extensions and modifications on the Stoney formula, for instance, the work by Injeti et al. [65] [66].
The reduced thickness area introduced in this thesis is only considered in a circular shape. Since the silicon elastic modulus is different in various directions, the optimal shape of the etched region would be elliptical, with the long axis along the more compact crystallography direction.
Moreover, the 3-D model of the die shear test to simulate the third mechanism of die failure would be helpful, as the source of the crack and its propagation path preference will be studied. The same 3D approach would improve the results for the other two mechanisms, as the assumption of plane strain in this dissertation is different from the real case.

List of Figures

List of Tables

Bibliography

[1] A. Corigliano, R. Ardito, C. Comi, A. Frangi, A. Ghisi, and S. Mariani, *Mechanics of Microsystems*. John Wiley & Sons, 2017.

[2] T. M. Adams and R. A. Layton, *Introductory MEMS*. Springer, 2014.

[3] B. E. Deal and A. Grove, "General relationship for the thermal oxidation of silicon," *Journal of Applied Physics*, vol. 36, no. 12, pp. 3770–3778, 1965.

[4] F. C. Mish, *Merriam-Webster's collegiate dictionary*. Merriam-Webster, 2004.

[5] M. J. Madou, *Fundamentals of microfabrication: the science of miniaturization*. CRC press, 2002.

[6] M. Tilli, M. Paulasto-Krockel, T. Motooka, and V. Lindroos, *Handbook of silicon based MEMS materials and technologies*. William Andrew, 2015.

[7] M. Esashi, "Wafer level packaging of MEMS," *Journal of Micromechanics and Microengineering*, vol. 18, no. 7, p. 073001, 2008.

[8] Q.-Y. Tong and U. Göesele, *Semiconductor wafer bonding: science and technology*. John Wiley & Sons, 1999.

[9] R. Stengl, T. Tan, and U. Gösele, "A model for the silicon wafer bonding process," *Japanese Journal of Applied Physics*, vol. 28, no. 10R, p. 1735, 1989.

[10] H. Takagi, R. Maeda, and T. Suga, "Wafer-scale spontaneous bonding of silicon wafers by argon-beam surface activation at room temperature," *Sensors and Actuators A: Physical*, vol. 105, no. 1, pp. 98–102, 2003.

[11] A. Reznicek, S. Senz, O. Breitenstein, R. Scholz, U. Gösele, F. Niedernostheide, and H. Schulze, "Electrical and structural investigation of bonded silicon interfaces," in *Semiconductor Wafer Bonding: Science, Technology, and Applications VI; Proceedings of the International Symposium*, vol. 2001, p. 114, The Electrochemical Society, 2002.

[12] J. Fan, G. Y. Chong, and C. S. Tan, "Study of hydrophilic Si direct bonding with ultraviolet ozone activation for 3D integration," *ECS Journal of Solid State Science and Technology*, vol. 1, no. 6, pp. P291–P296, 2012.

[13] D. I. Pomerantz, "Anodic bonding," Aug. 13 1968. US Patent 3,397,278.

[14] G. Wallis and D. I. Pomerantz, "Field assisted glass-metal sealing," *Journal of Applied Physics*, vol. 40, no. 10, pp. 3946–3949, 1969.

[15] A. Cozma and B. Puers, "Characterization of the electrostatic bonding of silicon and pyrex glass," *Journal of Micromechanics and Microengineering*, vol. 5, no. 2, p. 98, 1995.

[16] D.-J. Lee, Y.-H. Lee, J. Jang, and B.-K. Ju, "Glass-to-glass electrostatic bonding with intermediate amorphous silicon film for vacuum packaging of microelectronics and its application," *Sensors and Actuators A: Physical*, vol. 89, no. 1-2, pp. 43–48, 2001.

[17] F. Paschen, "Ueber die zum funkenübergang in luft, wasserstoff und kohlensäure bei verschiedenen drucken erforderliche potentialdifferenz," *Annalen der Physik*, vol. 273, no. 5, pp. 69–96, 1889.

[18] D. Sparks, G. Queen, R. Weston, G. Woodward, M. Putty, L. Jordan, S. Zarabadi, and K. Jayakar, "Wafer-to-wafer bonding of nonplanarized MEMS surfaces using solder," *Journal of Micromechanics and Microengineering*, vol. 11, no. 6, p. 630, 2001.

[19] R. Abbaschian and R. E. Reed-Hill, *Physical metallurgy principles*. Cengage Learning, 2008.

[20] F. Crnogorac, R. Birringer, R. Dauskardt, and F. Pease, "Aluminum-germanium eutectic bonding for 3D integration," in *2009 IEEE International Conference on 3D System Integration*, pp. 1–5, IEEE, 2009.

[21] S. Marauska, M. Claus, T. Lisec, and B. Wagner, "Low temperature transient liquid phase bonding of Au/Sn and Cu/Sn electroplated material systems for MEMS wafer-level packaging," *Microsystem Technologies*, vol. 19, no. 8, pp. 1119–1130, 2013.

[22] N. Bosco and F. Zok, "Critical interlayer thickness for transient liquid phase bonding in the Cu–Sn system," *Acta Materialia*, vol. 52, no. 10, pp. 2965–2972, 2004.

[23] K. Chu, Y. Sohn, and C. Moon, "A comparative study of Cu/Sn/Cu and Ni/Sn/Ni solder joints for low temperature stable transient liquid phase bonding," *Scripta Materialia*, vol. 109, pp. 113–117, 2015.

[24] C. Tan, R. Reif, N. Theodore, and S. Pozder, "Observation of interfacial void formation in bonded copper layers," *Applied Physics Letters*, vol. 87, no. 20, p. 201909, 2005.

[25] H. R. Tofteberg, K. Schjølberg-Henriksen, E. J. Fasting, A. S. Moen, M. M. Taklo, E. U. Poppe, and C. J. Simensen, "Wafer-level Au–Au bonding in the 350–450 $^{\circ}$ C temperature range," *Journal of Micromechanics and Microengineering*, vol. 24, no. 8, p. 084002, 2014.

[26] A. K. Panigrahi, S. Bonam, T. Ghosh, S. G. Singh, and S. R. K. Vanjari, "Ultra-thin Ti passivation mediated breakthrough in high quality Cu-Cu bonding at low temperature and pressure," *Materials Letters*, vol. 169, pp. 269–272, 2016.

[27] H. Kon, M. Uomoto, and T. Shimatsu, "Room temperature bonding of wafers in air using Au-Ag alloy films," in *2014 4th IEEE International Workshop on Low Temperature Bonding for 3D Integration (LTB-3D)*, pp. 28–28, IEEE, 2014.

[28] L. Yifang, C. Daner, L. Liwei, Z. Gaofeng, Z. Jianyi, W. Lingyun, and S. Daoheng, "Glass frit bonding with controlled width and height using a two-step wet silicon etching procedure," *Journal of Micromechanics and Microengineering*, vol. 26, no. 3, p. 035018, 2016.

[29] X. Chen, P. Yan, J. Tang, G. Xu, and L. Luo, "Development of wafer level glass frit bonding by using barrier trench technology and precision screen printing," *Microelectronic Engineering*, vol. 100, pp. 6–11, 2012.

[30] H. Kind, E. Gehlen, M. Aden, A. Olowinsky, and A. Gillner, "Laser glass frit sealing for encapsulation of vacuum insulation glasses," *Physics Procedia*, vol. 56, pp. 673–680, 2014.

[31] R. Knechtel, M. Wiemer, and J. Frömel, "Wafer level encapsulation of microsystems using glass frit bonding," *Microsystem Technologies*, vol. 12, no. 5, pp. 468–472, 2006.

[32] G. G. Stoney, "The tension of metallic films deposited by electrolysis," *Proceedings of the Royal Society of London. Series A, Containing Papers of a Mathematical and Physical Character*, vol. 82, no. 553, pp. 172–175, 1909.

[33] L. Freund, J. Floro, and E. Chason, "Extensions of the Stoney formula for substrate curvature to configurations with thin substrates or large deformations," *Applied Physics Letters*, vol. 74, no. 14, pp. 1987–1989, 1999.

[34] L. B. Freund and S. Suresh, *Thin film materials: stress, defect formation and surface evolution*. Cambridge university press, 2004.

[35] C. Dresbach, A. Krombholz, M. Ebert, and J. Bagdahn, "Mechanical properties of glass frit bonded micro packages," *Microsystem Technologies*, vol. 12, no. 5, pp. 473–480, 2006.

[36] B. Bhushan, *Introduction to tribology*. John Wiley & Sons, 2013.

[37] X. Li and B. Bhushan, "Measurement of fracture toughness of ultra-thin amorphous carbon films," *Thin Solid Films*, vol. 315, no. 1-2, pp. 214–221, 1998.

[38] W. C. Oliver and G. M. Pharr, "Measurement of hardness and elastic modulus by instrumented indentation: Advances in understanding and refinements to methodology," *Journal of materials research*, vol. 19, no. 1, pp. 3–20, 2004.

[39] I. N. Sneddon, "The relation between load and penetration in the axisymmetric Boussinesq problem for a punch of arbitrary profile," *International journal of engineering science*, vol. 3, no. 1, pp. 47–57, 1965.

[40] M. F. Doerner and W. D. Nix, "A method for interpreting the data from depth-sensing indentation instruments," *Journal of Materials research*, vol. 1, no. 4, pp. 601–609, 1986.

[41] X. Li and B. Bhushan, "A review of nanoindentation continuous stiffness measurement technique and its applications," *Materials characterization*, vol. 48, no. 1, pp. 11–36, 2002.

[42] W.-G. Jiang, J.-J. Su, and X.-Q. Feng, "Effect of surface roughness on nanoindentation test of thin films," *Engineering Fracture Mechanics*, vol. 75, no. 17, pp. 4965–4972, 2008.

[43] M. Miller, C. Bobko, M. Vandamme, and F.-J. Ulm, "Surface roughness criteria for cement paste nanoindentation," *Cement and Concrete Research*, vol. 38, no. 4, pp. 467–476, 2008.

[44] A. C. Fischer-Cripps and D. Nicholson, "Nanoindentation. mechanical engineering series," *Appl. Mech. Rev.*, vol. 57, no. 2, pp. B12–B12, 2004.

[45] B. Boettge, C. Dresbach, A. Graff, M. Petzold, and J. Bagdahn, "Mechanical characterization and micro structure diagnostics of glass frit bonded interfaces," *ECS Transactions*, vol. 16, no. 8, pp. 441–448, 2008.

[46] T.-R. Hsu, "Reliability in MEMS packaging," in *2006 IEEE International Reliability Physics Symposium Proceedings*, pp. 398–402, IEEE, 2006.

[47] S. Mariani, A. Ghisi, A. Corigliano, and S. Zerbini, "Multi-scale analysis of MEMS sensors subject to drop impacts," *Sensors*, vol. 7, no. 9, pp. 1817–1833, 2007.

[48] "Test method standard for microcircuits," standard, United States of America Department of Defence, Mar. 1995.

[49] K. B. Kim, J. Kim, C. W. Park, J. H. Kim, and N. K. Min, "Glass-frit bonding of silicon strain gages on large thermal-expansion-mismatched metallic substrates," *Sensors and Actuators A: Physical*, vol. 282, pp. 230–236, 2018.

[50] Z. Sun, D. Pan, J. Wei, and C. Wong, "Ceramics bonding using solder glass frit," *Journal of electronic materials*, vol. 33, no. 12, pp. 1516–1523, 2004.

[51] K. Fu, Y. Li, L. Yin, and J. Zhang, "Effect of CuO on laser absorption in glass to glass laser bonding," in *2014 15th International Conference on Electronic Packaging Technology*, pp. 484–488, IEEE, 2014.

[52] A. Corigliano, "Formulation, identification and use of interface models in the numerical analysis of composite delamination," *International Journal of Solids and Structures*, vol. 30, no. 20, pp. 2779–2811, 1993.

[53] T. Rabczuk, G. Zi, S. Bordas, and H. Nguyen-Xuan, "A geometrically non-linear three-dimensional cohesive crack method for reinforced concrete structures," *Engineering Fracture Mechanics*, vol. 75, no. 16, pp. 4740–4758, 2008.

[54] M. Johar, M. S. E. Kosnan, and M. N. Tamin, "Cyclic cohesive zone model for simulation of fatigue failure process in adhesive joints," in *Applied Mechanics and Materials*, vol. 606, pp. 217–221, Trans Tech Publ, 2014.

[55] O. Allix and P. Ladevèze, "Interlaminar interface modelling for the prediction of delamination," *Composite structures*, vol. 22, no. 4, pp. 235–242, 1992.

[56] G. T. Camacho and M. Ortiz, "Computational modelling of impact damage in brittle materials," *International Journal of solids and structures*, vol. 33, no. 20-22, pp. 2899–2938, 1996.

[57] L. Margolin, "A generalized Griffith criterion for crack propagation," *Engineering fracture mechanics*, vol. 19, no. 3, pp. 539–543, 1984.

[58] J. Dienes, "Comments on "a generalized griffith criterion for crack propagation" by LG Margolin," *Engineering Fracture Mechanics*, vol. 23, no. 3, pp. 615–617, 1986.

[59] R. Sills and M. Thouless, "Cohesive-length scales for damage and toughening mechanisms," *International Journal of Solids and Structures*, vol. 55, pp. 32–43, 2015.

[60] M. Ebert and J. Bagdahn, "Determination of residual stress in glass frit bonded MEMS by finite element analysis," in *5th International Conference on Thermal and Mechanical Simulation and Experiments in Microelectronics and Microsystems, 2004. EuroSimE 2004. Proceedings of the*, pp. 407–412, IEEE, 2004.

[61] Å. Sandvand, E. Halvorsen, K. E. Aasmundtveit, and H. Jakobsen, "Influence of glass-frit material distribution on the performance of precision piezoresistive MEMS pressure sensors," *IEEE Transactions on Components, Packaging and Manufacturing Technology*, vol. 5, no. 11, pp. 1559–1566, 2015.

[62] A. Masolin, P.-O. Bouchard, R. Martini, and M. Bernacki, "Thermo-mechanical and fracture properties in single-crystal silicon," *Journal of Materials Science*, vol. 48, no. 3, pp. 979–988, 2013.

[63] M. A. Hopcroft, W. D. Nix, and T. W. Kenny, "What is the Young's modulus of silicon?," *Journal of microelectromechanical systems*, vol. 19, no. 2, pp. 229–238, 2010.

[64] S. Barnat, H. Frémont, A. Gracia, and E. Cadalen, "Evaluation by three-point-bend and ball-on-ring tests of thinning process on silicon die strength," *Microelectronics Reliability*, vol. 52, no. 9-10, pp. 2278–2282, 2012.

[65] S. S. Injeti, N. Vyas, and R. K. Annabattula, "Modified stoney's equation with anisotropic substrates undergoing large deformations," *arXiv preprint arXiv:1712.07974*, 2017.

[66] G. C. Janssen, M. M. Abdalla, F. Van Keulen, B. R. Pujada, and B. Van Venrooy, "Celebrating the 100th anniversary of the stoney equation for film stress: Developments from polycrystalline steel strips to single crystal silicon wafers," *Thin Solid Films*, vol. 517, no. 6, pp. 1858–1867, 2009.